BIFROST – analyser designs

	Name	Role/Title
Owner	Rasmus Toft-Petersen Liam Whitelegg	Lead Instrument Scientist, Bifrost Lead Instrument Engineer, Bifrost
Reviewer	Ken Andersen, Klaus Habicht Arno Hiess,	NSS Lead Instrument Scientist Group leader – Helmholtz-Zentrum Berlin Head of Scientific Activities Division
Approver	Shane Kennedy	NSS Project Leader

TABLE OF CONTENT **PAGE**

1. INTRODUCTION 4
1.1 Purpose of the document 4
1.2 Definitions, acronyms and abbreviations 5
1.3 References 5
2. PRINCIPLE OF THE BIFROST SECONDARY SPECTROMETER SYSTEM 6
2.1 Horizontally flat analysers in a vertical scattering setup 7
2.2 Prismatic analyser concept 9
3. ARRANGEMENT OF THE SPECTROMETER CHANNELS AND THE TANK DESIGN 10
4. METHODOGOLY FOR CALCULATING THE ANALYSER GEOMETRY 13
5. MCSTAS SIMULATIONS: VALIDATION AND EVALUATION OF PERFORMANCE 16
5.1 Spatial focusing 17
5.2 Energy resolution 20
5.2.1 Sample size effects 21
5.2.2 Detector spacing 22
5.3 Effect of mosaicity 23
5.3.1 Spatial distribution 23
5.3.2 Resolution function and intensity 24
6. GRAPHITE MOUNTING 25
7. SUMMARY 27
8. APPENDIX A – SUMMARY PLOTS 29
8.1 Summary plots for 2.7 meV 29
8.2 Summary plots for 3.2 meV 30
8.3 Summary plots for 3.8 meV 32
8.4 Summary plots for 4.4 meV 33
8.5 Summary plots for 5 meV 35

LIST OF TABLES

No table of figures entries found.

LIST OF FIGURES

Figure 1: a) Illustration of the Bifrost analyser/detector geometry. b) Illustration of the continued divergence of the scattered neutrons off the analysers. Position sensitivity of the detectors allows effectively A4 sensitivity. 6

Figure 2: Illustration of the effect of mosaicity in a backscattering projection, sin(a5) =1. At the edge of the detector, the analyser area contributing to the observed signal is half that of the point in the analyser scattering plane. 8

Figure 3: Principle of distance collimation used to select three distinct energies of scattering from the analyser scattering plane. 9

Figure 4 - Section View through the Beam Plane 10

Figure 5 - Final Analyser Arrangement (left) and the Final Detector Arrangement (right) 11

Figure 6 - Contingency Added to Cross-talk Shielding 11

Figure 7 - Section View through a Q Channel 12

Figure 8: Principle behind the reduction in vertical coverage 13

Figure 9: Illustration of Rowland geometry 14

Figure 10: Illusatration of analyser geometry 14

Figure 11: Calculated analyser geoemtry, symmetric 5 meV 15

Figure 12: Calculated geoemtry, short 2.7 meV 15

Figure 13: McStas geometry 16

Figure 14: Principle for scanning the curvature in McStas 17

Figure 15: Example of spatial focusing, symmetric 5.0 meV channel. The red lines denote the ideal detector positions. 18

Figure 16: Curvature scan of the width projection on the PSD y-axis. A gaussian optimum is clearly identifiable. For this analyser – 5.0 meV symmetric – the optimum tilt angle 0.33 is clearly confirmed. 18

Figure 17: Example of summary plot from the curvature scan of the 5.0 meV analyser, where the caluclated optimum is clearly reproduced. ASP is short for analyser scattering plane. 19

Figure 18: Distribution of neutron energies on a single triplet, 5.0 meV – short, using a sample size of 0.5x0.5x0.5 mm. The splitting of energies is clearly evident 21

Figure 19: Energy distribution of the scattering off a 5 meV analyser (short), for various cube dimensions of sample size.....21

Figure 20: Relationsship between the single tube resolution and the triple tube resolution as a function of sample size - for a 5 meV short channel. 22

Figure 21: Intensity distribution of a short 5 meV analyser, as a function of tube separation. 22

Figure 22: Spread of scattered neutrons off the 2.7 meV analyser as a function of mosaicity. 23

Figure 23: Spread of scattered neutrons off the 5.0 meV analyser as a function of mosaicity 24

Figure 24: Energy distribution of the scattered beam off the 2.7 meV analyser, as a function of mosaicity. 24

Figure 25: Energy distribution of the scattered beam off the 5.0 meV analyser, as a function of mosaicity. 25

26 - Clip used on the CAMEA instrument 26

27 - PG Mounting Concept.....27

1. INTRODUCTION

1.1 Purpose of the document

This document aims to describe the BIFROST analyser design in detail, for the Preliminary Design Review (PDR). The purpose of the review is to approve the analyser/detector geometries in relation to their scientific rationale and performance. This allows the BIFROST team to fix the overall geometry of the secondary spectrometer (SSP) and issue a call for tender for the HOPG crystals to be used. The detailed engineering design of the analyser holders, the tank and the crosstalk shielding is not a part of this review, only the scattering geometry itself.

Throughout this document, knowledge of analyser basics are assumed.

This document contains:

- A detailed description of the scattering geometry of the special type of BIFROST secondary spectrometer geometry.
- A description of the of the stacking choices of the BIFROST analysers and detectors, providing the rationale for the overall secondary spectrometer design, coupling these choices to the tank design, crosstalk shielding and economic boundary conditions.
- A detailed description of the methodology for calculating the analyser geometries

- Description of the McStas simulation setup and results used to double check and verify the analyser/detector geometries.

- Evaluation of mounting possibilities for the analyser crystals and the budget.

1.2 Definitions, acronyms and abbreviations

ABBREVIATION	EXPLANATION OF ABBREVIATION
PBS	Product Breakdown Structure
NOSG	Neutron Optics and Shielding Group
BTS	Beam Transport and Conditioning System
SES	Sample Exposure System
SCS	Scattering Characterization System
GUI	Graphical user interface
CLI	Command line interface
EPICS	Experimental Physics and Industrial Control System
PSS	Personnel Safety System
PSI	Paul Scherrer Institute
LLB	Laboratorie Leon Brillouin
IFE	Institut for Energiteknik
KU	University of Copenhagen
DTU	Technical University of Denmark

1.3 References

[1] PhD Thesis, Jonas Okkels Birk
[2] J. O. Birk, et al., Prismatic analyser concept for neutron spectrometers, Rev. Sci. Instr 85 113908 (2014)
[3] F. Groitl, et al. CAMEA – a novel multiplexing analyser for neutron spectroscopy, Rev. Sci instruments, 87, 035109 (2016)
[4] M. Marton, et. al. Prototype of the novel CAMEA concept—A backend for neutron spectrometers, Rev Sci Instr, 89, 015105 (2018)
[5] M. Marko, Analytical calculations for CAMEA, BIFROST proposal report, attached to Indico page.

2. PRINCIPLE OF THE BIFROST SECONDARY SPECTROMETER SYSTEM

The secondary spectrometer of BIFROST employs a range of new ways to use analysers in neutron spectroscopy as compared to conventional triple-axis spectroscopy in order to maximize overall spatial angle coverage, while retaining high flexibility in terms of both Q- and energy resolution. These are:

1. Employing a scattering geometry in the vertical plane, enabling the use of multiple Q-channels simultaneously.
2. Exploiting the transparency of HOPG at neutron energies below 5 meV, to place analysers behind one another downstream the sample position, enabling multi energy analysis in a single Q-channel.
3. Employing flat analysers in the horizontal direction perpendicular to the sample-analyser axis, with position sensitive detectors (along that same axis). This allows continuous sensitivity to scattering angle (A4 in conventional TAS terms). See figure 1.
4. Employing the prismatic analyser concept, described in [2]. This is basically utilizing the distance collimation. A small sample (as in BIFROST), a large HOPG mosaicity and a long analyser-detector distance allows the detector size to determine the energy resolution. A triplet of 1D detectors then allows the possibility of choosing between a narrow energy band (1 tube) and a wide energy band (3 tubes) of the channel in question. See figure 1.

Since 1 and 2 are now routinely employed in existing and future backends (FlatCone, MultiFLEXX, E2, Bambus, Camea, etc), these are assumed well-known by the reader and will not be elaborated here.

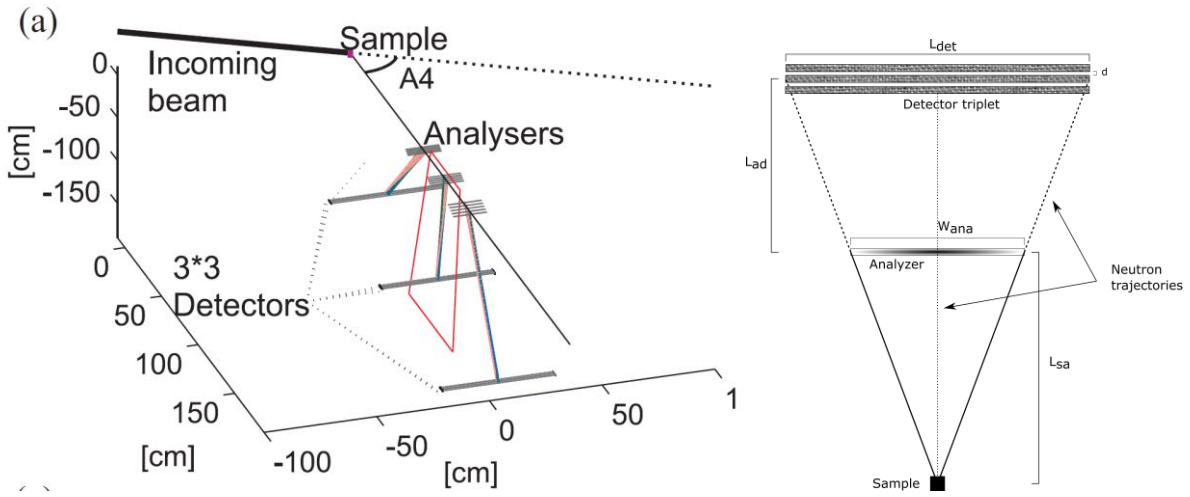

Figure 1: a) Illustration of the Bifrost analyser/detector geometry. b) Illustration of the continued divergence of the scattered neutrons off the analysers. Position sensitivity of the detectors allows effectively A4 sensitivity.

Instead, we move on to describe principles 3 and 4, and their consequences for the secondary spectrometer design

2.1 Horizontally flat analysers in a vertical scattering setup

Figure 1 illustrates the principle behind the analyser/detector geometry of Bifrost. For any given A4-angle, several analysers situated behind one another downstream from sample scatters neutrons out of the horizontal plane, at an angle corresponding to the energy selected by the analyser in question.

The analysers are *flat horizontally*, perpendicular to the sample-analyser axis. Since the analyser mosaicity is much smaller than the average analyser coverage angle, this allows for the A4 discrimination when using an extended 1D detector, see [3, 4, 5].

However, due to the resulting conservation of divergence with respect to the sample-analyser axis, this causes the diffracted beam from the analysers to *widen* as it reaches the detector. A neutron following the path from the sample to the *center* of the analyser, stays with the plane defined by the sample position, the centre of the analyser and the centre of the detector (see figure 1 left). However, a neutron trajectory reaching the *edge* of the analyser moves further away from the aforementioned plane after the analyser diffraction process (second trajectory on figure 1 left). Thus, the detectors corresponding to any analyser in this geometry needs to be substantially longer than the analyser is wide, as figure 1 shows. The relationship between detector length and analyser width is straightforwardly connected to the ratio between L_{sa} and L_{ad}:

$$L_{det} = \frac{(L_{sa} + L_{ad})}{L_{sa}} \cdot W_{ana}$$

This simple expression disregards the mosaicity of the analysers. In principle, one could catch the mosaicity-induced tail of the diffracted signal from the analysers by increasing the detector length. However, the tail of the scattering off the analysers is hard to use scientifically, since the A4-resolution narrows in the tail. This is true because a smaller A4-range (area) of analyser contributes to the scattering on the detector edge. This is illustrated in figure 2, in the simple backscattering geometry (a5 = 90 degrees). The centre point of the detector sees a scattering contribution from both sides of the analyser scattering plane, due to the mosaicity. The FWHM of that contribution is decided by the analyser mosaicity. However, at the edge of the detector, only half the A4-range of that of the centre reaches the detector, and thus the A4-resolution is substantially reduced.

The solution to this is not to increase the detector length, as that would increase the range of variable A4-resolution. Rather, the analyser width should be increase to allow the same Q-resolution through the entire A4-range to be covered by the analyser, by design. See figure 2. If we let W_{bla} denote the nominal width, disregarding mosaicity. The full width of the analyser ensuring full illumination of the corresponding detector is then denoted W_{full}.

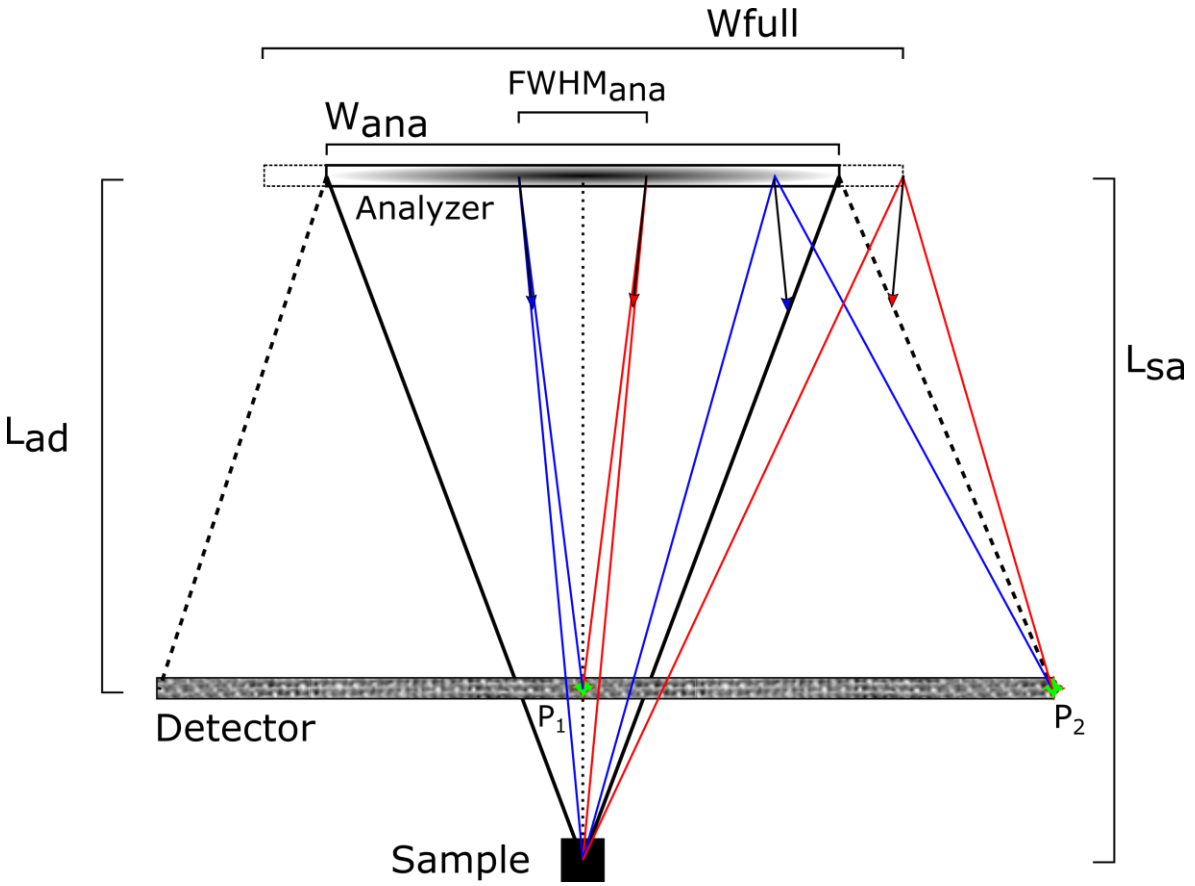

Figure 2: Illustration of the effect of mosaicity in a backscattering projection, sin(a5) =1. At the edge of the detector, the analyser area contributing to the observed signal is half that of the point in the analyser scattering plane.

The full width of the analyser can be calculated by calculating the A4-range contributing to the scattering on a single detector point $FWHM_{ana}$:

$$W_{full} = W_{ana} + FWHM_{ana} = W_{ana} + 2\tan(\xi) \cdot L_{ad} \cdot \sin(a5)$$

The sin(a5) dependence is due to the effect of the HOPG (002) axis becoming more and more perpendicular to the neutron path, as the take-off angle a5 is decreased. This reduces the mosaicity-induced widening and thereby $FHWM_{ana}$.

In summary, for a given desired analyser angular coverage, the nominal width of the analyser – W_{ana} – can be calculated. Using the distances L_{sa} and L_{ad}, the corresponding detector active length is calculated. Knowing the mosaicity of the analysers, the real width of the analyser – W_{full} – is then deduced. Thus, L_{det} and W_{full} determines the extent of both detector and analyser perpendicular to the analyser scattering plane.

Finally, it should be noted that using an analyser which is flat perpendicular to the analyser scattering plane, the take-off angle a5 will be very slightly dependent on a4. However, as this is a minor effect and since this can be taken into account in the software, this effect will not be treated here. It is well described in the PhD thesis of Jonas Okkels Birk [1], chapter 4.4.10.2, page 81.

2.2 Prismatic analyser concept

The prismatic analyser concept is thoroughly described in reference [2], and we refer to that article for an in-depth explanation.

Usually, on conventional TAS machines, the sample is rather large, the analyser mosaicity is small, and a wide detector is situated close to said analyser. This maximizes the signal intensity, and it renders the energy resolution partly dependent on analyser mosaicity. On BIFROST however, the sample size is small, the distances between sample/analyser and analyser/detector are long and the analyser mosaicity is large. Therefore, several small detectors at the detector positions each probe a unique and non-overlapping Bragg angle in the analyser scattering plane, and hence a unique and non-overlapping energy, see figure 3. This allows for a high degree of flexibility of the backend resolution, which match perfectly to the highly flexible primary spectrometer resolution of Bifrost.

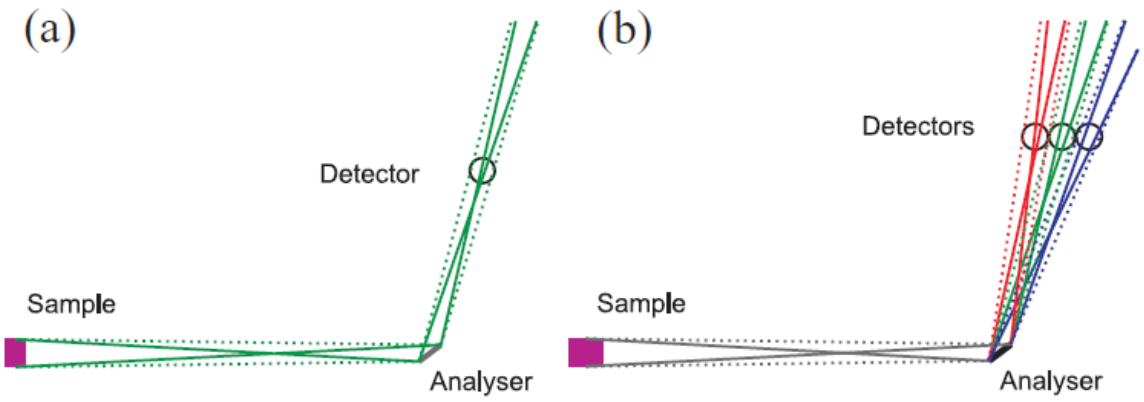

Figure 3: Principle of distance collimation used to select three distinct energies of scattering from the analyser scattering plane.

This principle only works when the mosaicity is large enough to cover all used detectors. In our case, 1 degree mosaicity is enough and is to be used in all analysers. This rather large mosaicity also have the advantage of being rather inexpensive.

In general, analytical calculations of both A4- and energy resolution of this type of analyser geometry can be found in reference [5]

3. ARRANGEMENT OF THE SPECTROMETER CHANNELS AND THE TANK DESIGN

When looking to position the analysers and detectors, several rounds of design and calculation iterations were required. In order to minimise costs, the aim was to position the analysers as close to the sample position as reasonably feasible, keeping both analyser area and detector lengths down. The components shown in the figure below determined the minimum analyser distance feasible.

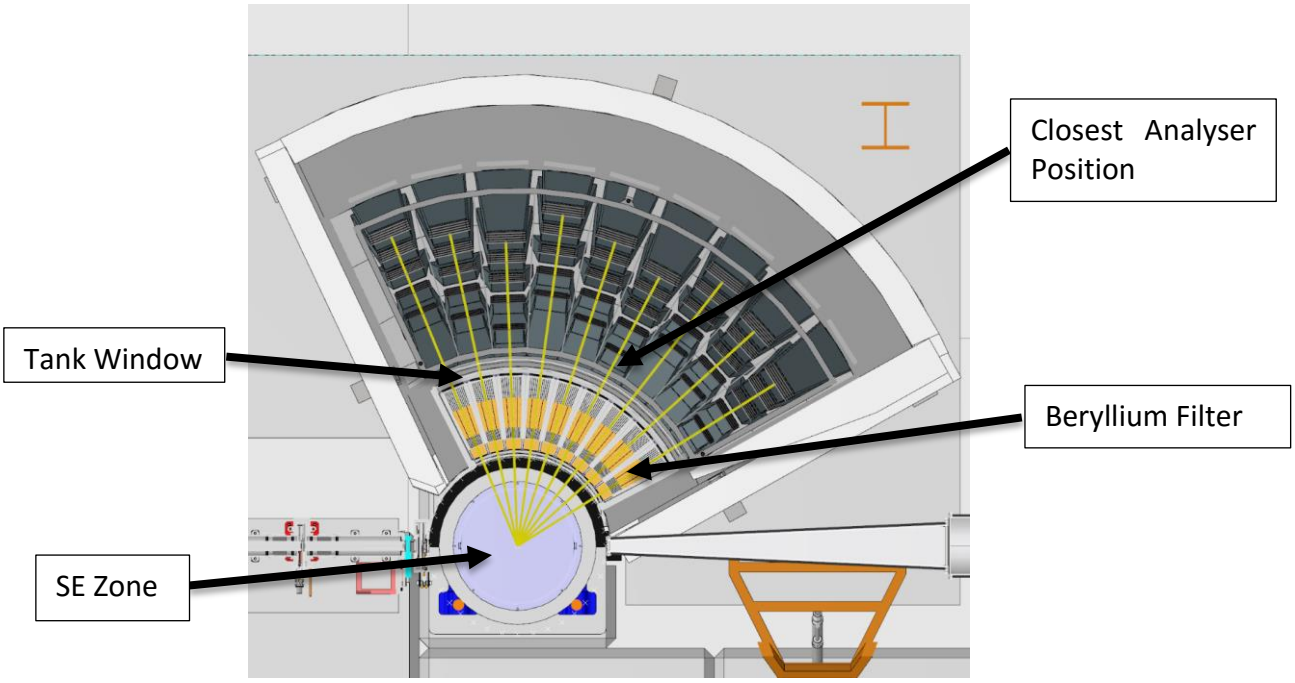

Figure 4 - Section View through the Beam Plane

As Bifrost will look to employ cryomagnets at the sample position, an Ø900mm exclusion zone has been enforced at the sample position to ensure space for both current and future equipment. We then require significant space for the beryllium filter and the vacuum tank, leaving the closest viable analyser position at around 1.1m from the sample. This, in combination with our high-level requirement to provide full 90-degree coverage in two settings, set the base to start iterating.

The first iterative step was to ensure that we had space to fit the detectors on the base of the tank (in air). As stated in the previous section, the detectors need to be considerably longer than the analysers are wide, in some cases more than twice as long. In addition, the 1D-detector tubes have an additional 'dead' length of roughly 20 mm, due to the way the anode wire is mounted. On top of that, the tubes need high voltage connectors that will increase the space taken up by a detector triplet even further.

Initial designs showed the analysers would have to move back significantly as the detectors clashed with each other. As this increased costs, we started to look into staggering the detectors until they could fit. It was found that moving to 9 channels of 5.2° and introducing a “triple stagger”, as shown below, provided enough space for the detectors whilst minimising the distance to the furthest analyser.

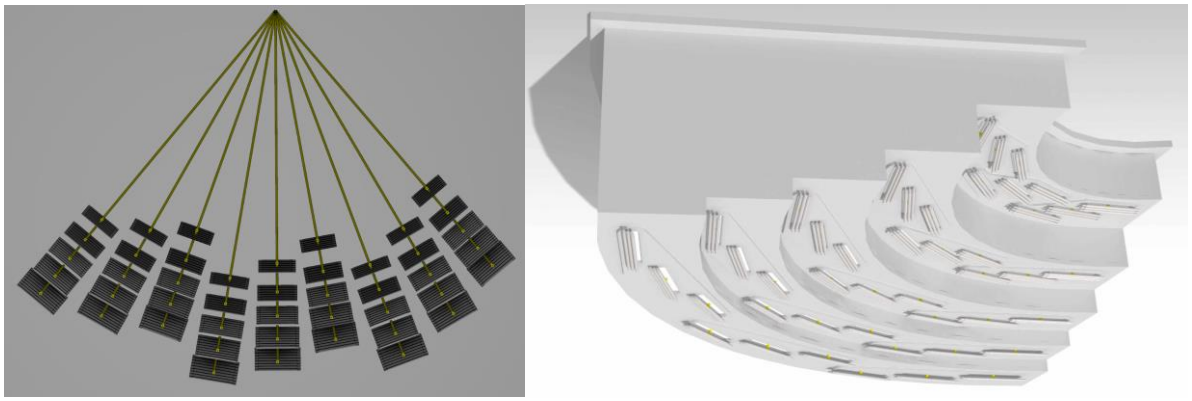

Figure 5 - Final Analyser Arrangement (left) and the Final Detector Arrangement (right)

Whilst the triple stagger solved a clash issue, the detectors would now have to sit on 15 different vertical planes in order to maintain the Rowland geometry. In order to keep the tank geometry simple and minimise air gaps, we decided to position all of the detectors of the same energy on the same vertical plane. This means that 2/3rds of the analysers are slightly asymmetric but the tank is only stepped 5 times.

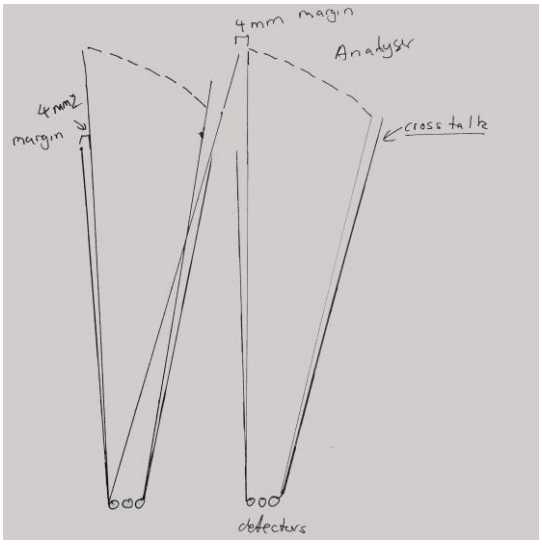

Figure 6 - Contingency Added to Cross-talk Shielding

The final stage of iteration was to then ensure there that there is no cross talk between the different analysers. To counter this, we will position absorbing tubes that shroud the divergence profile of each analyser to its corresponding detector. The tubes will be constructed from absorbing sheets and be constrained within the vacuum tank. Due to the

potential mis-alignments and manufacturing tolerances involved, we decided to add 4mm of contingency to the cross talk, as shown above, by adjusting the analyser positions accordingly.

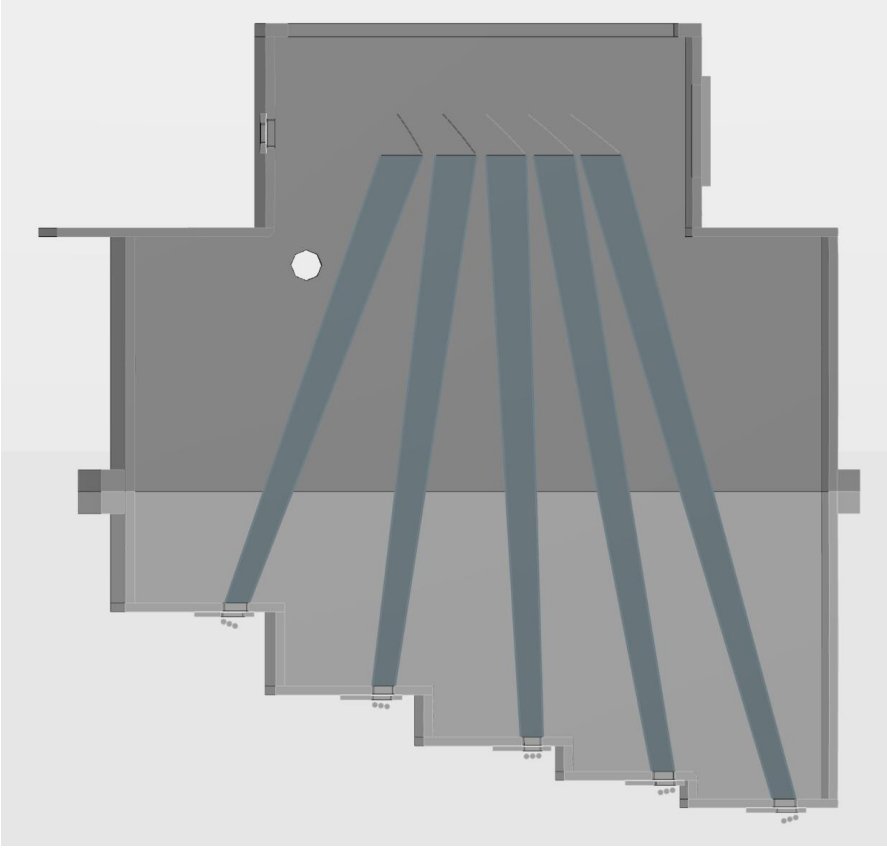

Figure 7 - Section View through a Q Channel

	A4-coverage [deg.]	L_{sa} [mm]	L_{ad} [mm]	# blades	Vertical coverage [deg.]
2.7 meV - short	5.2	1100	1189	7	2
2.7 meV – symm.	5.2	1189	1189	7	2
2.7 meV - long	5.2	1276	1189	7	2
3.2 meV - short	5.2	1238	1314	7	1.8372
3.2 meV – symm.	5.2	1314	1314	7	1.8372
3.2 meV - long	5.2	1388	1314	7	1.8372
3.8 meV - short	5.2	1342	1418	9	1.6861
3.8 meV – symm.	5.2	1418	1418	9	1.6861
3.8 meV – long	5.2	1493	1418	9	1.6861
4.4 meV - short	5.2	1443	1520	9	1.5669
4.4 meV – symm.	5.2	1520	1520	9	1.5669
4.4 meV – long	5.2	1595	1520	9	1.5669
5.0 meV - short	5.2	1544	1622	9	1.47
5.0 meV – symm.	5.2	1622	1622	9	1.47
5.0 meV – long	5.2	1697	1622	9	1.47

Table 1: Chosen analyser geometries

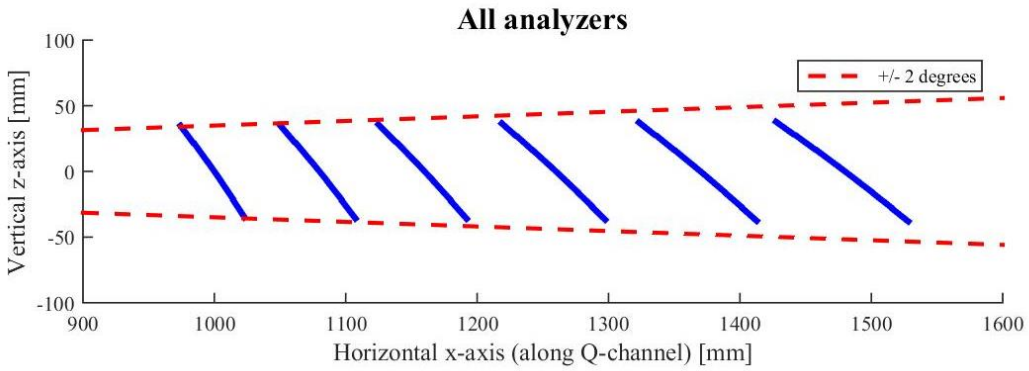

Figure 8: Principle behind the reduction in vertical coverage

Lastly, we have opted to have a constant vertical Q-coverage, rather than a constant vertical angular coverage. This creates a uniform vertical resolution and saves some PG.

4. METHODOGOLY FOR CALCULATING THE ANALYSER GEOMETRY

In the vertical plane, the Bifrost analysers are curved. This is of course to optimize energy resolution and achieve point-to-point focusing.

Since Bifrost is designed for extreme magnetic fields, the vertical coverage of the analysers is limited to the acceptance angle of a standard Oxford cryomagnet, +/- 2 degrees. Along with the engineer-defined scattering geometry and the horizontal A4-coverage number, one can proceed to work on the analyser geometry. The basis for this is the well-known Rowland circle, containing the sample, analyser centre point and the detector centre point. This is shown below:

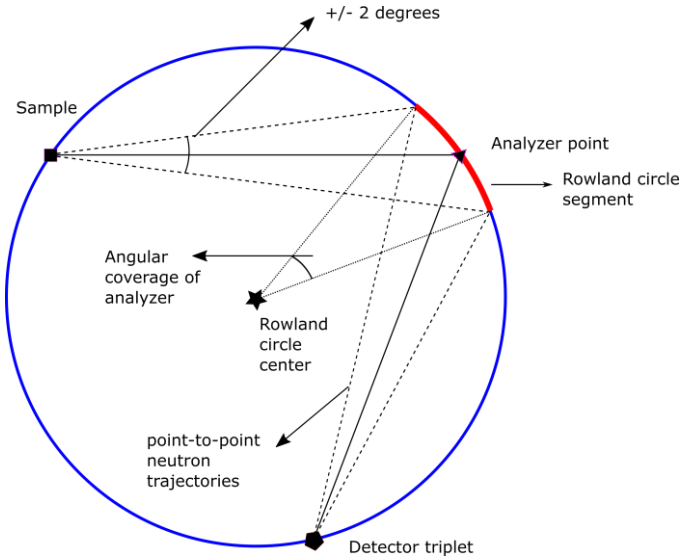

Figure 9: Illustration of Rowland geometry

The chosen vertical angular coverage defines an analyser arc on the Rowland circle (Red arc). This is the arc in the analyser scattering plane on which to centre the analyser blades – it defines the placement of the blades that allows achieving both a uniform take-off angle on the blades and point-to-point focusing.

What remains to define the analyser geometry is to define the number of blades to be used for the analyser in question, and the spacing between them. The inter-blade spacing should be chosen to maximize HOPG area, within practical reason. We have chosen the number of blades such as to ensure that the blade width is comparable to or slightly larger than the detector width: between 12 and 15 mm. This is a decision adopted from the PSI CAMEA project, and we did not look into which blade width would be optimal

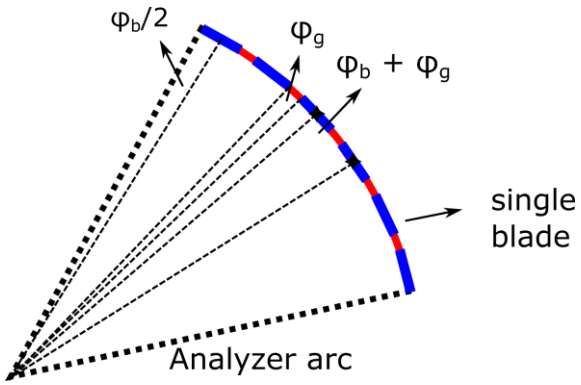

Figure 10: Illustration of analyser geometry

As the figure above suggests, the blade width is known from the analyser arc length on the Rowland circle, the number of blades and the spacing between them. The blade positions are calculated as the figure suggests. The blade width and blade spacing take up certain angles

on the analyser arc, ϕ_b and ϕ_g. These angles can be easily use to uniformly distribute the blades on the analyser arc as the figure suggests, with an angular separation between blades of $\phi_b + \phi_g$.

Once the geometry is defined, and the blade positions fixed, the point-to-point geometry of Bifrost allows for a simple calculation of the angles of reflection, finishing the design of the analyser. This is automatized in a matlab-script, the result of which is shown in the two examples below.

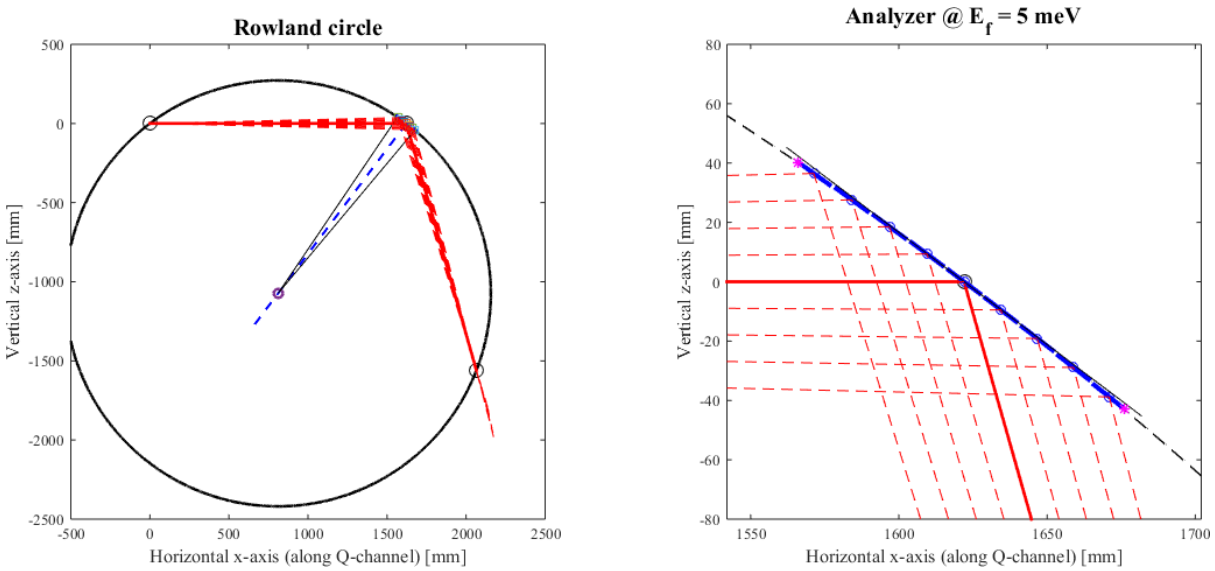

Figure 11: Calculated analyser geometry, symmetric 5 meV

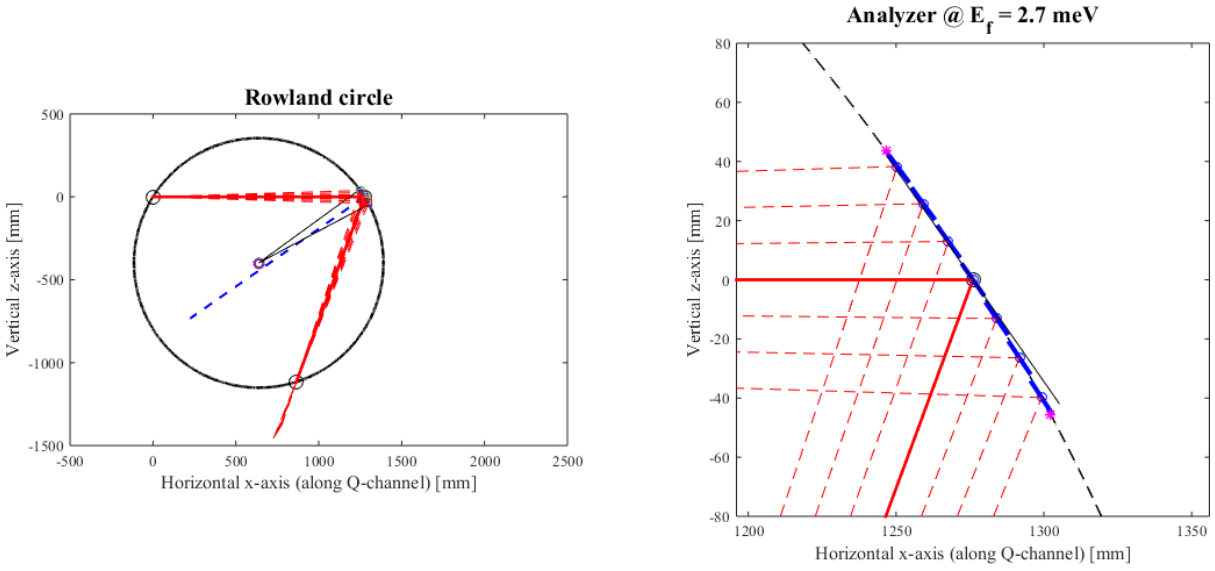

Figure 12: Calculated geometry, short 2.7 meV

Using an automatic analyser geometry script, one can engage in iterative processes with engineers and optimize placement and coverage with respect to cross talk shielding and tank design.

Moving on to the McStas simulation.

5. MCSTAS SIMULATIONS: VALIDATION AND EVALUATION OF PERFORMANCE

The chosen McStas geometry is a simple one. As a sample position, we have made a source component at the origin, a cube of variable side length (sample size). It focuses the emitted neutrons in a cone larger than the analyser, with a wavelength band of 1 Å centered on the Bragg wavelength of the analyser in question.

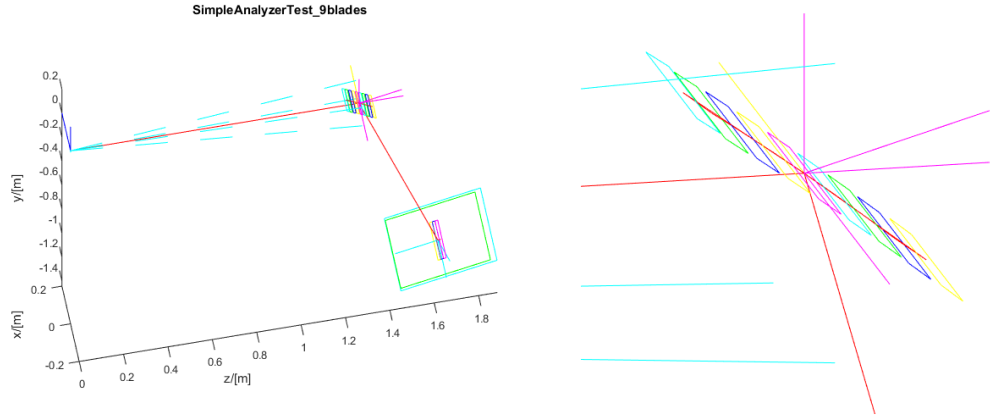

Figure 13: McStas geometry

At the nominal A5 of the analyser, we place a range of detectors:

1) First, the triplet of tubes with the length calculated as in the previous section and a width of 0.5 inch. The spacing between the tubes is a variable

2) The we have a very large PSD, that serves the purpose of tracking all scattering off the analyser

3) Finally, we have an equally large Tof/energy monitor, which serves the purpose of tracking the overall energy band reflected off the analyser, and not merely the band measured by the detector triplet. This proves that there is no attenuation in the wavelength band relevant to the adjacent analysers.

The only scan parameter of the analyser is the curvature. The way this is changed is merely by changed the step in take-off angle between each blade, using a single parameter for the analyser as a whole, see below.

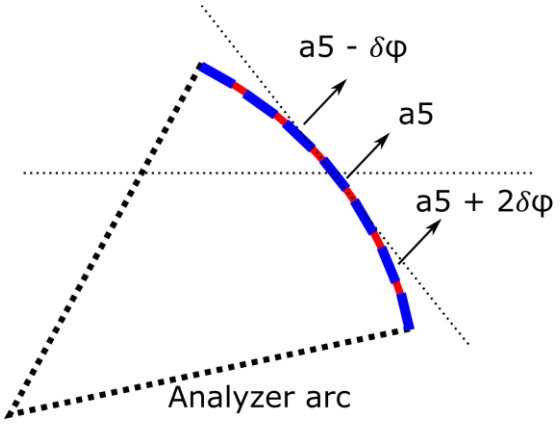

Figure 14: Principle for scanning the curvature in McStas

Scanning the parameter $\delta\varphi$ is a simple way of check that the calculated take-off angles are correct, check what kind of tolerances are acceptable and check that the energy resolution is optimized.

Once this is done for all analysers, we check the effects of sample size and mosaicity for a select few of the analysers, as these effects are generic.

For all blades, a HOPG mosaicity of 1 degree have been chosen, both to ensure distance collimation and for price reasons.

5.1 Spatial focusing

The spatial focusing can be examined via the large PSD data set. On the figure below, two examples are shown. On the left, the defocused beam with all blades having the same take-off angle and on the right the focused beam. The length is in this case defined along the detector tube, the direction perpendicular to the analyser scattering plane (ASP), and it is unaffected by the focusing.

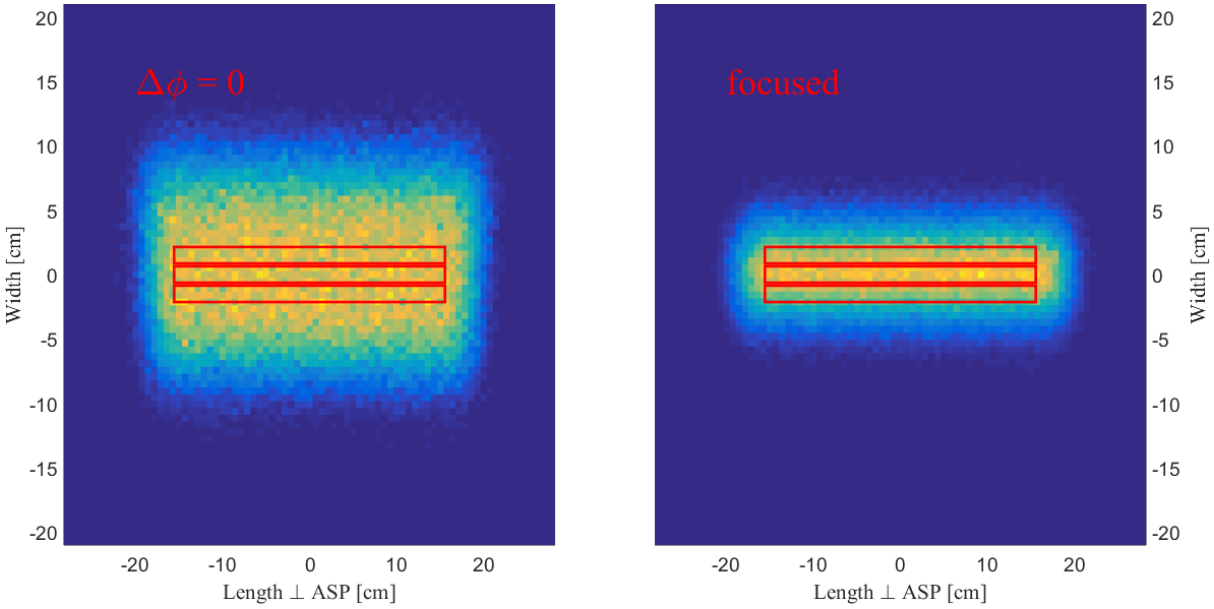

Figure 15: Example of spatial focusing, symmetric 5.0 meV channel. The red lines denote the ideal detector positions.

On the other hand, the width is altered by focusing and by analysing the curvature-dependent projection of the signal on the width-axis (y-axis), and confirm the optimum and compare with the detector extent. Below are those projections as a function of blade tilt angle, where an optimum is clearly identifiable.

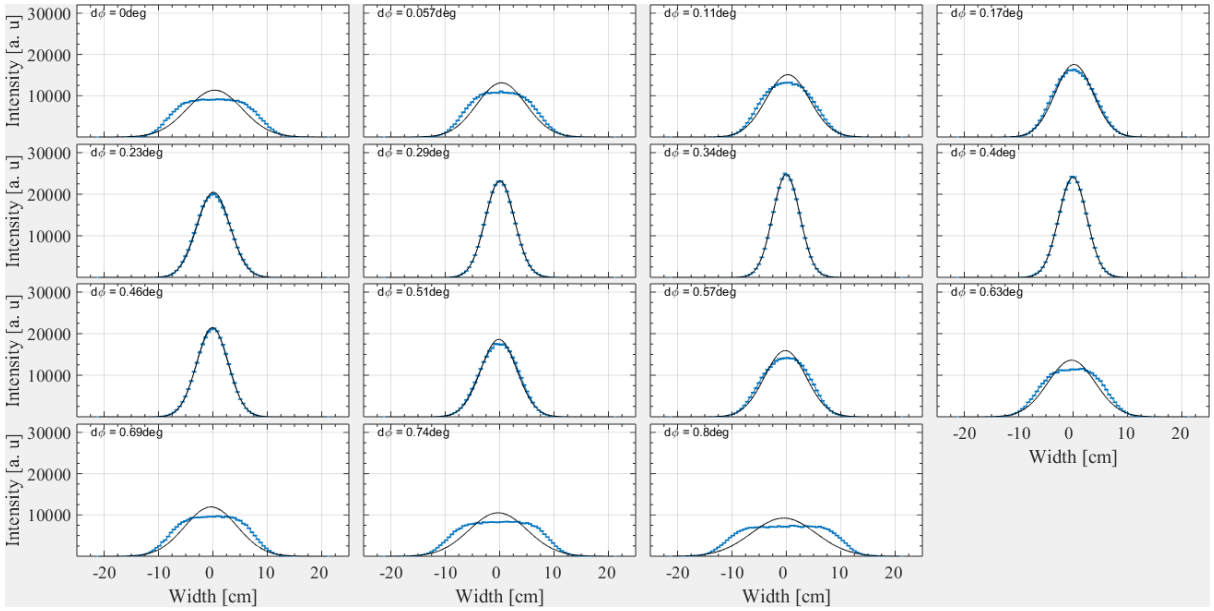

Figure 16: Curvature scan of the width projection on the PSD y-axis. A Gaussian optimum is clearly identifiable. For this analyser – 5.0 meV symmetric – the optimum tilt angle 0.33 is clearly confirmed.

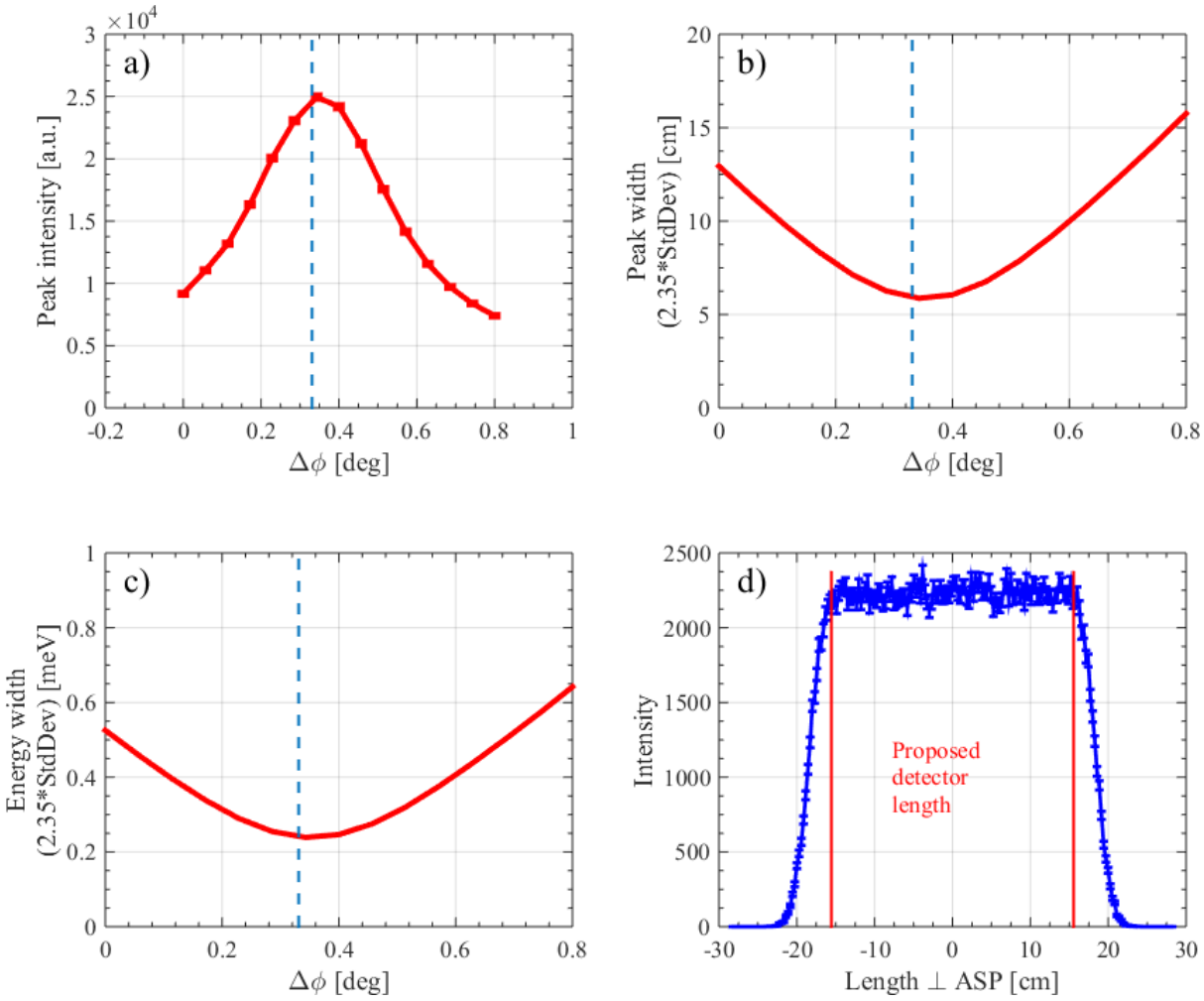

Figure 17: Example of summary plot from the curvature scan of the 5.0 meV analyser, where the calculated optimum is clearly reproduced. ASP is short for analyser scattering plane.

Figure 17 a and b, shows the peak intensity and width as a function of blade tilt angle. The width is given in FWHM calculated numerically, as 2.35*StdDev, where StdDev is the numerically calculated standard deviation. This enable straightforward comparison of different distributions.

Figure 17 c shows the spread of neutron energies reaching the very large energy monitor, a measure of the energy band reflected off the analyser as a whole. This serves to confirm that the analyser energy intervals are appropriate and the effect of blade misalignment

Figure 17 d is a projection of the PSD signal onto the detector axis. The red lines show the propose detector length. This serves to make sure that the full detector length is illuminated.

A summary plot similar to figure 17 is produced for all 15 analyser geometries, and given in Appendix A.

Lastly, we illustrate how much of the overall analyser signal is picked up by the detectors, shown in the figure below for the two extreme cases of 2.7 and 5.0 meV analyser energy.

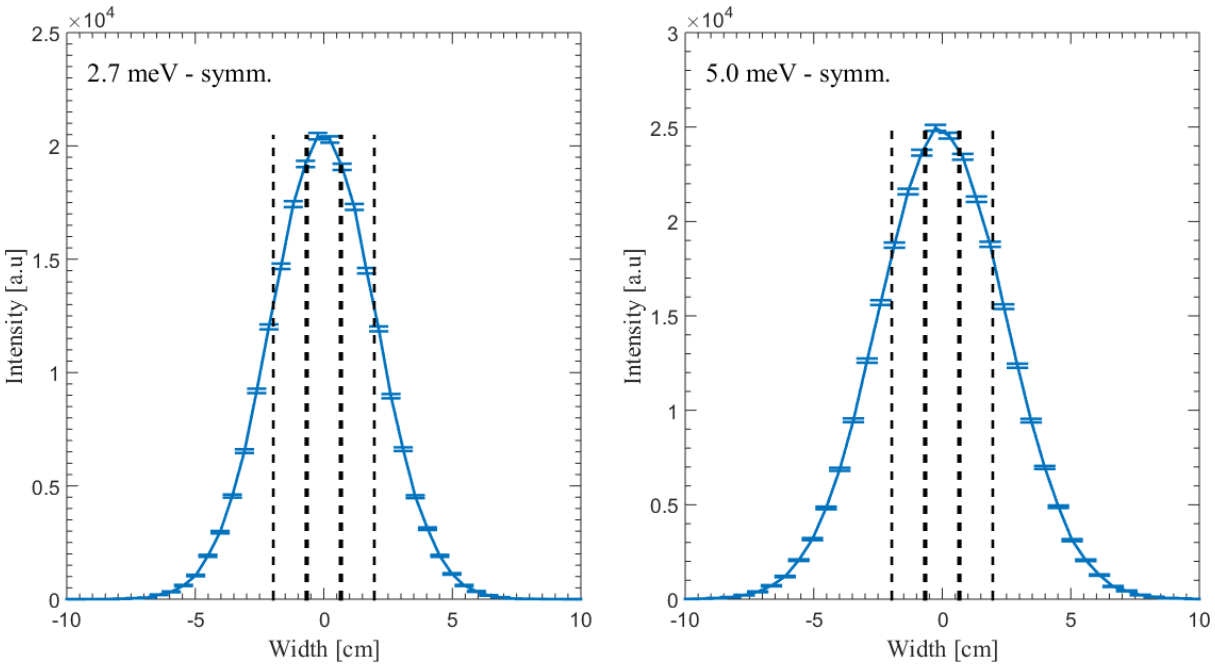

As evident, only about half of the scattered neutrons off the analysers hit detectors. This is a natural consequence of distance collimation, where the detector size needs to be smaller than the spread of neutrons from the analyser. It is possible to arrange more than three detectors side by side, as 5-7 detectors would cover the whole scattered distribution. However, the marginal benefit of the extra detectors strongly decrease after the 3 detectors and a future upgrade to 5-7 detectors per channels is currently so improbable, that we have chosen not to design for it. Doing so would mean a larger distance between analysers and a much larger tank, bearing a high cost on day 1 with no immediate benefit.

5.2 Energy resolution

Since we are distance collimated, the energy band detected by each detector is independent on curvature. Therefore a single tube detects a narrower energy band than the triplet as a whole and the energy band of a single tube is much narrow than usually known from triple axis machines.

Figure 13 shows the energy distribution of neutrons hitting the short 5.0 meV triplet, each detector represented by a different colour. As evident, the FWHM of a single tube band is roughly 50-60 µeV, while the FWHM of the triplet as a whole – the sum of the 3 tubes – has a FWHM of 150 µeV, more in line with usual TAS values.

Of course, the primary spectrometer resolution has an equal impact on the overall resolution. The resolution of the primary spectrometer is within the single tube energy bands of all analysers, allowing for full flexibility.

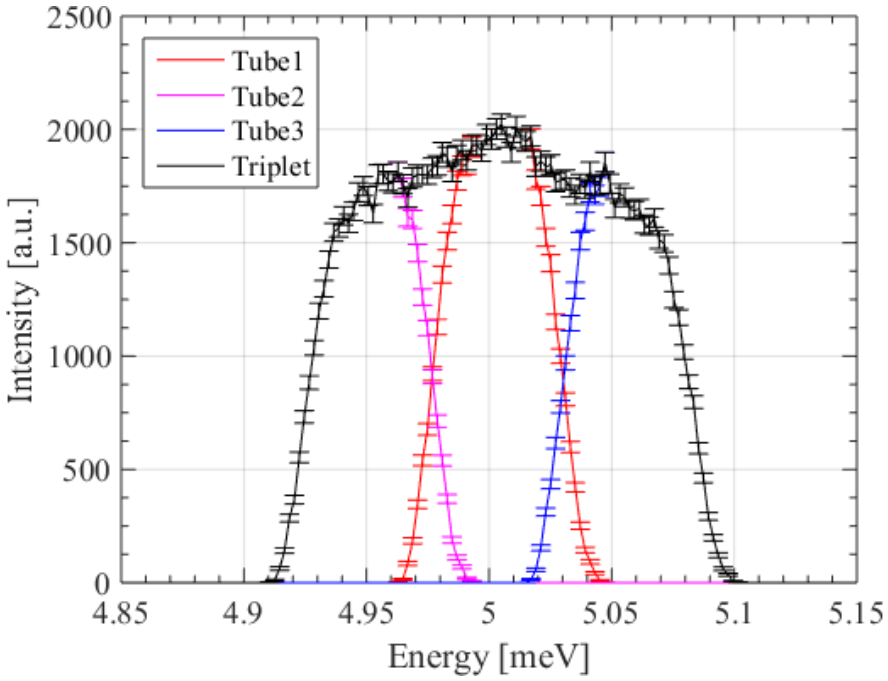

Figure 18: Distribution of neutron energies on a single triplet, 5.0 meV – short, using a sample size of 0.5x0.5x0.5 mm. The splitting of energies is evident

Two other parameters influence the resolution function of the secondary spectrometer, namely the sample size and the detector tube separation.

5.2.1 Sample size effects

The energy resolution of an analyser setup is a function of the take-off angle, the mosaicity, and the two acceptance angles between sample/analyser and analyser/detector, respectively.

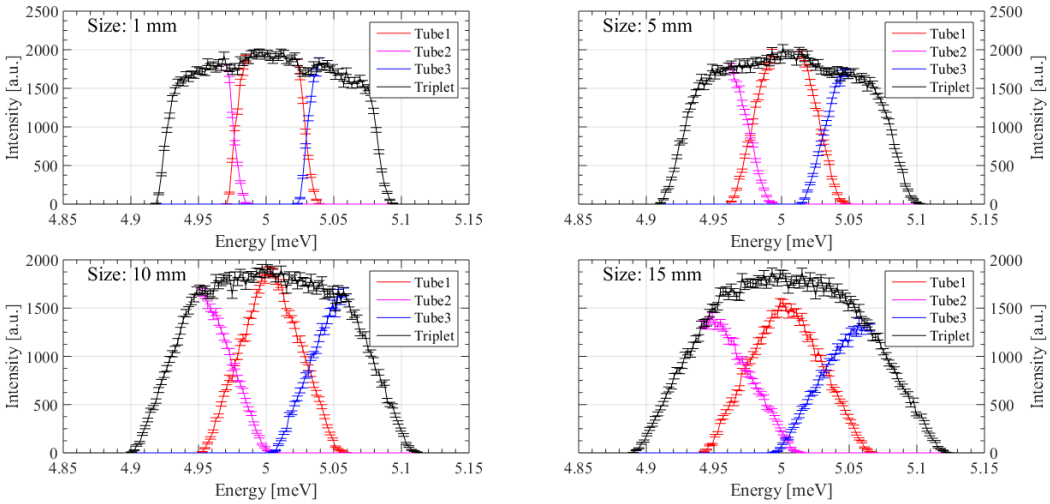

Figure 19: Energy distribution of the scattering off a 5 meV analyser (short), for various cube dimensions of sample size

Therefore, the larger sample size will invariably increase the energy resolution as the Bragg angles accepted by each detector is increased and allowed by the mosaicity. As the sample size increases, the resolution of the single tube relative to the triplet will increase, see the figure below.

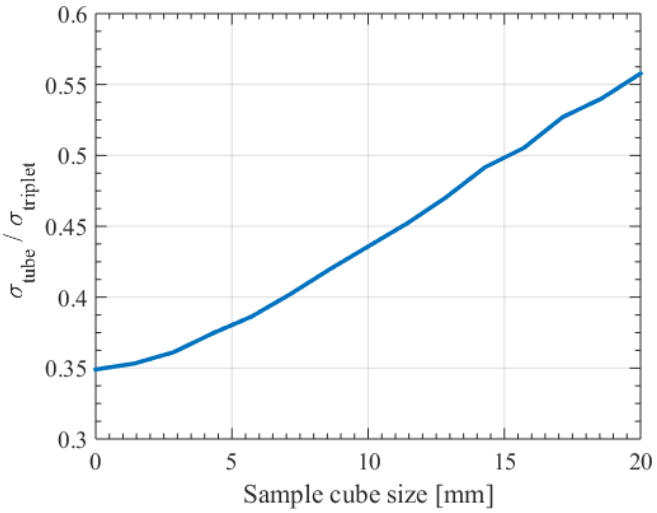

Figure 20: Relationship between the single tube resolution and the triple tube resolution as a function of sample size - for a 5 meV short channel.

Therefore, at large samples the primary spectrometer resolution needs to be tuned accordingly to maximize flux.

5.2.2 Detector spacing

The distance between detector tubes within the triplet has an impact on the energies probed, due to the change in Bragg angle. See below.

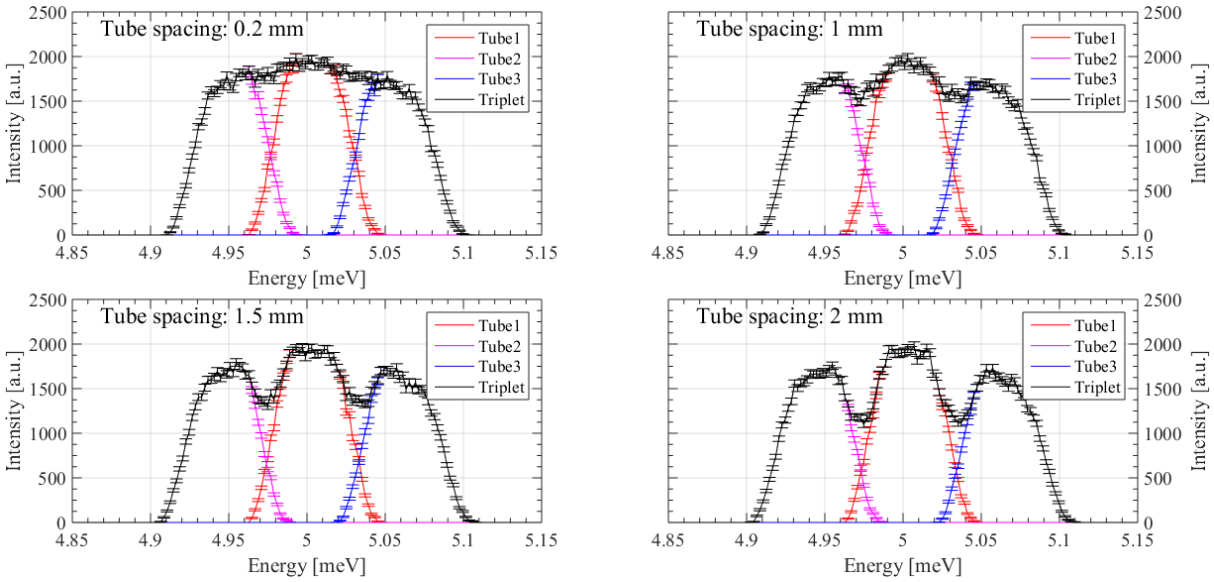

Figure 21: Intensity distribution of a short 5 meV analyser, as a function of tube separation.

Allowing for a space between detectors, allows for a clearer separation of probed energy transfers. However, one simple mode of Bifrost operation would be to add the signal from all three tubes in a coarse resolution setting. One would then have simple A4 values to deal with for each Ef, allowing for Bifrost to resemble a simple TAS spectrometer.

5.3 Effect of mosaicity

Changing the mosaicity changes the spread of neutrons from the analysers, of course mostly in the analyser scattering plane. This spread does not change the energy distribution, but it changes the shape of the secondary spectrometer resolution function. Below, the spread of neutrons and the resulting energy distribution is examined.

5.3.1 Spatial distribution

The figure below shows the width of the scattered beam off the closest analyser at 2.7 meV as a function of mosaicity.

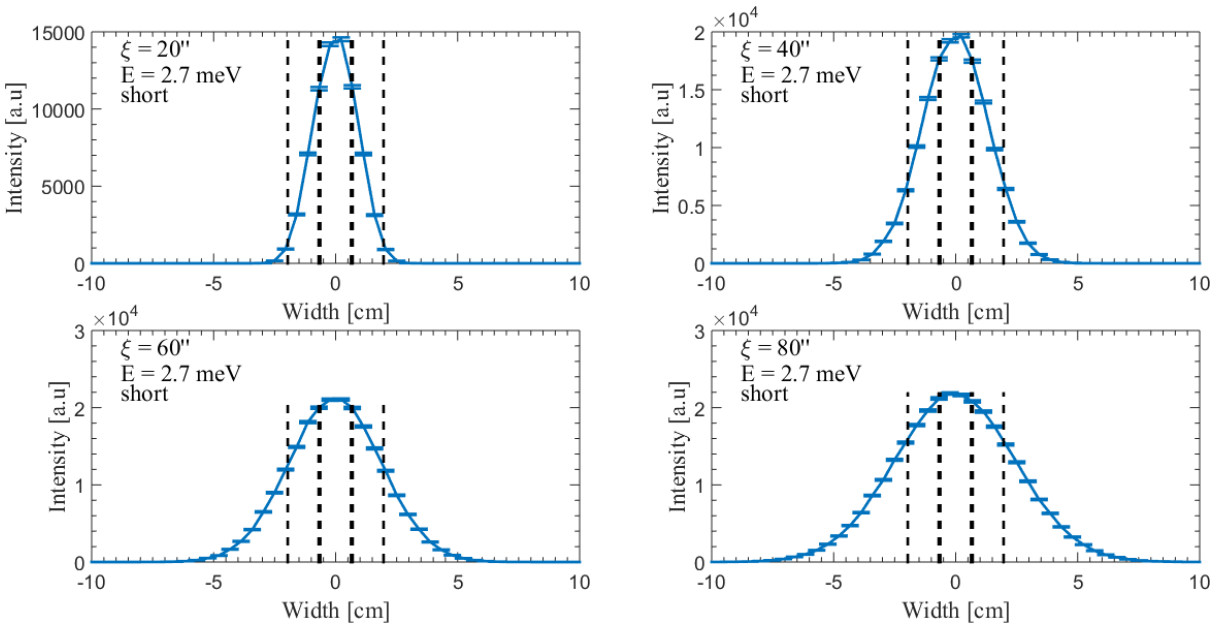

Figure 22: Spread of scattered neutrons off the 2.7 meV analyser as a function of mosaicity.

Assuming three detector tubes, the optimal mosaicity looking at the spot width projected onto the analyser scattering plane (ASP) is the chosen one, 60 ''. This allows 70 % of neutrons to reach detectors and allows a high peak flux on all three tubes.

The plot below shows a similar plot of beam spread versus mosaicity, for a 5 meV analyser with a considerable longer distance between analyser and detector. Therefore, the scattered beam off the analysers spreads out more. For these far analysers, it might improve background to tighten the width by using a slightly smaller mosaicity – 40 - 50 ''.

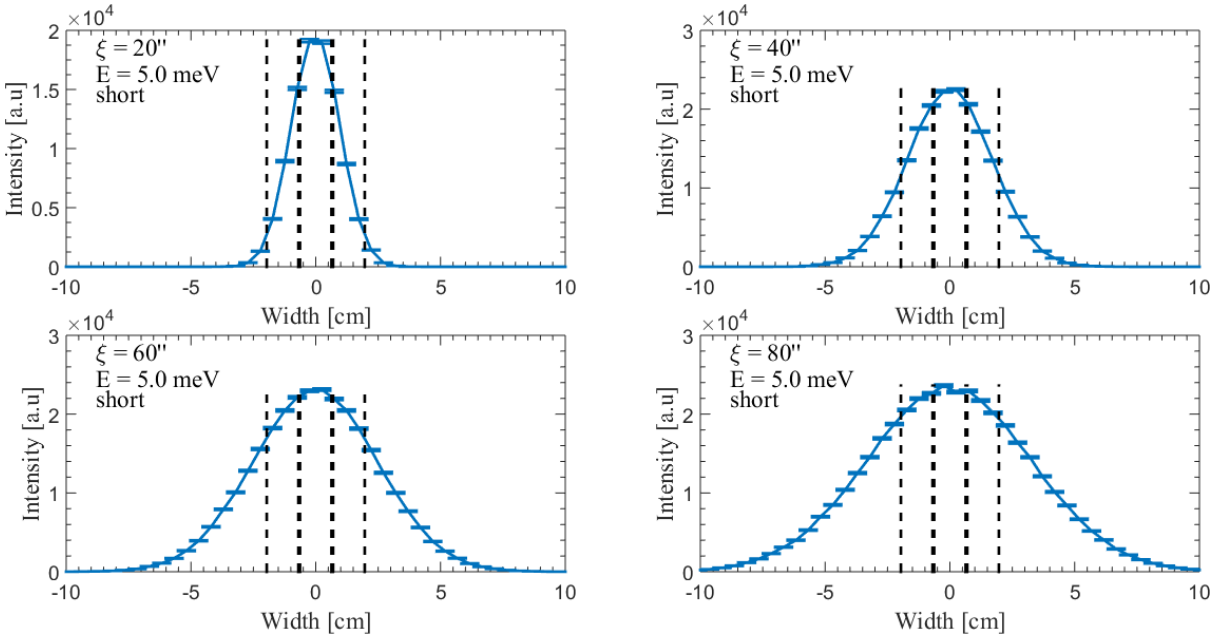

Figure 23: Spread of scattered neutrons off the 5.0 meV analyser as a function of mosaicity

A tighter beam spread also have an impact on the resolution function shape.

5.3.2 Resolution function and intensity

Below you can see a plot of the energy distribution on the various detector tubes on the 2.7 meV analyser.

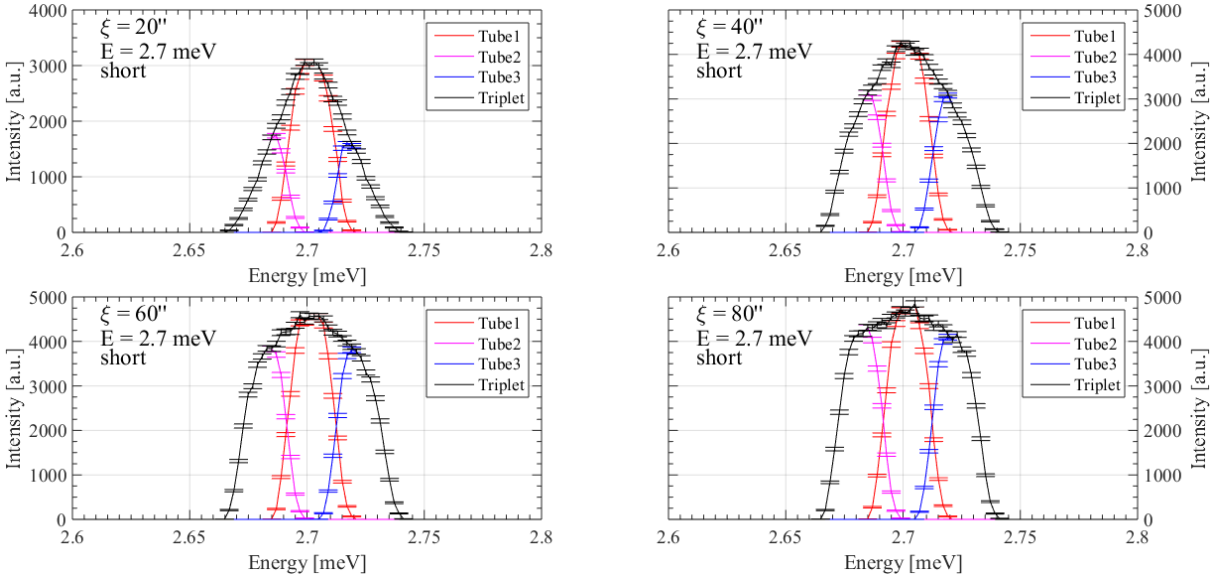

Figure 24: Energy distribution of the scattered beam off the 2.7 meV analyser, as a function of mosaicity.

As evident on figure 24, the resolution function of the two side tubes becomes asymmetric with a very tight mosaicity. However, with 60 degree mosaicity, the detector acceptance angle is much smaller than the angular spread of the analyser in question. Therefore the resolution function of all three tubes are symmetric and with similar intensity.

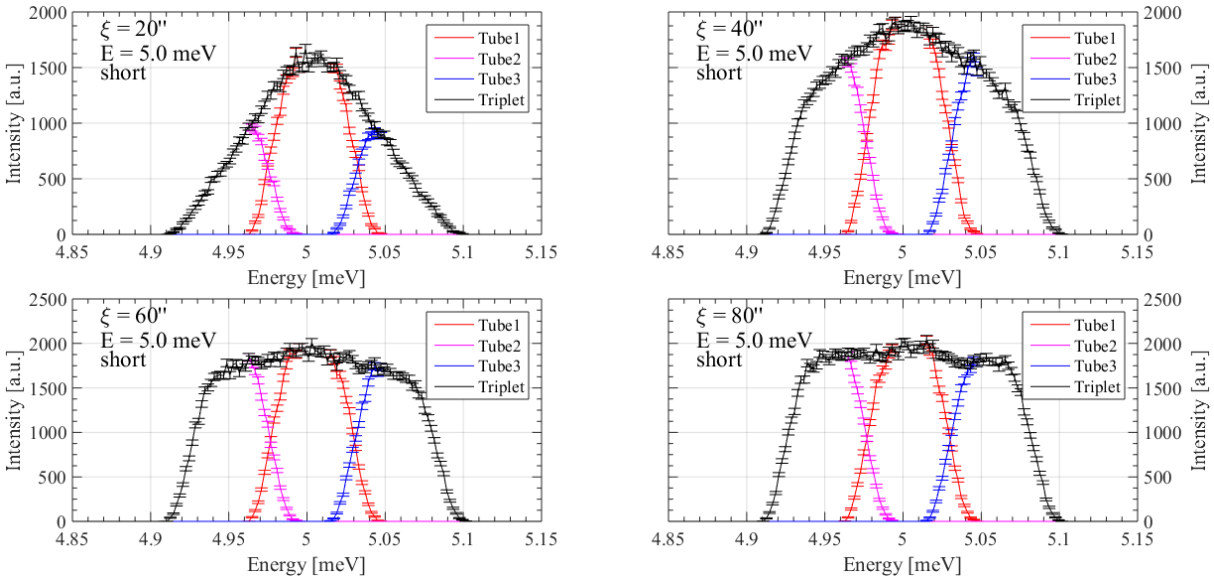

Figure 25: Energy distribution of the scattered beam off the 5.0 meV analyser, as a function of mosaicity.

The same effect appears is the case for the 5.0 meV analyser.

One thing, which is not addressed by the McStas simulations, is the reflectivity of the HOPG as a function of both thickness and mosaicity. There may be a higher intensity when choosing a narrow graphite mosaicity, since the reflectivity might go up. This cannot be simulated using the simple McStas components used here, and we will investigate the impact of reflectivity using analytical methods and previous experimental experience later on.

6. GRAPHITE MOUNTING

Whilst investigating different analyser geometries, numerous mounting options have also been investigated. The options considered by the team are outlined below;

- Screw Mounting – Two titanium/aluminium screws are used to secure each crystal to a backing silicon wafer. This method is relative economic but the mosaicity around the screw holes can deteriorate.
- Mounting with Shellac – The PG is glued on to silicon wafers. We were unable to get quotes on this and a thin, controlled layer of shellac would be required to minimise absorption.
- Indium Soldering – Indium is sputtered on to the PG crystal and then soldered on to the silicon wafer. There were concerns over the effects of Indium within the beam and this option costs double of the screw mounting (200k€).
- Direct Bonding – The PG crystals are directly bonded onto silicon wafers through a hot pressing process. This is a new and seemingly perfect option but would cost more than the PG crystals themselves (450k€).
- Clip Mounting – Aluminium clips are used to fix the PG crystals to the silicon wafer. This is the cheapest and lowest risk option as it is a proven method (CAMEA, PSI), but

adds more aluminium to the beam path and slightly increases the distance between PG blades.

Of the options above, Direct Bonding and Indium Soldering are effectively ruled out for budgetary reasons. Mounting with Shellac would require development work and it is believed that the background would be greater than that of the two physical mounting options. This left us with a choice between Clip or Screw Mounting and due to the risks of deterioration in the mosaicity of the PG, have chosen Clip Mounting.

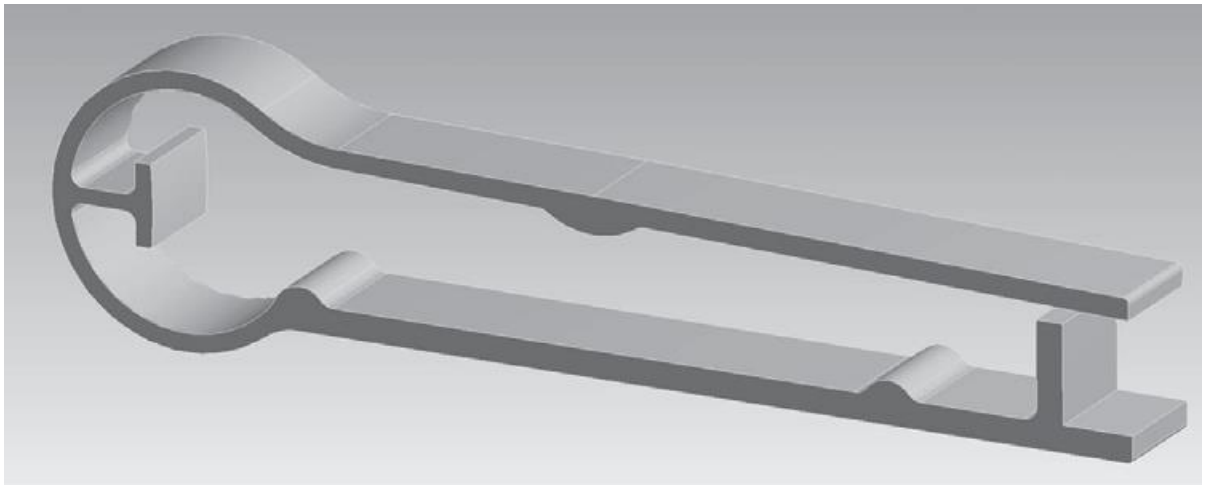

Figure 26 - Clip used on the CAMEA instrument

So we will use 2 (or 3) 90° cut crystals per blade, each clipped onto a silicon wafer at two positions. In order to minimise the gaps between the blades, the clips will be staggered between neighbouring blades. The silicon wafer will be miscut by 4°(at least) with respect to <111> to minimise reflections and each silicon wafer will then be clipped on to an aluminium holder, with cross talking shielding positioned wherever feasible.

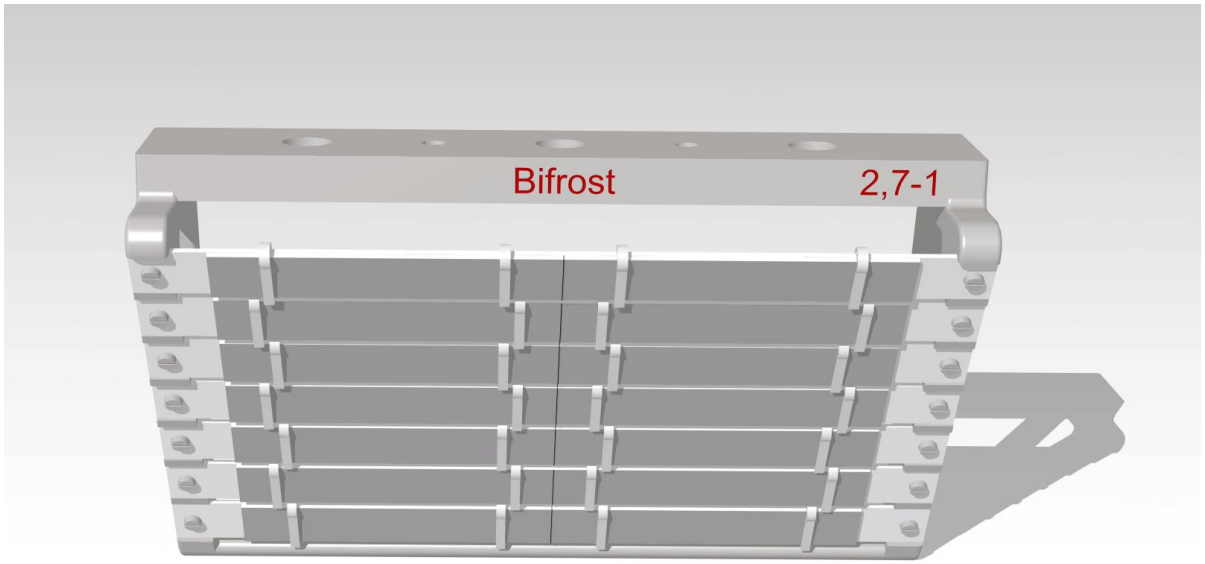

Figure 27 - PG Mounting Concept

7. SUMMARY

In summary, the analyser geometries are well understood and the simulated performances are as expected. The energy resolutions of the single tube and the triplet tube are given in the table below. Elastic line resolution of the instrument is variable between 20 and 150 ueV, and for a given k_f, a factor of three difference is attainable for small samples.

The energy resolution is calculated numerically from the simulated energy distribution data (like in figure 18) to ease comparison, using a box function approximation:

$$\Delta E = 2.35 \cdot \sigma \cdot \frac{8 \cdot \log 2}{12}$$

Where 2.35 is the conversion factor from standard deviation to FWHM, and the last factor is a conversion factor from Gaussian FWHM to Box function FWHM.

The current simulation setup makes it hard to directly evaluate the A4 resolution from the simulations, but the A4 simulation can be calculated numerically, using the formula:

$$\Delta A4 = \frac{\sqrt{8/12 \cdot \log 2 \cdot sw^2 + (2 \cdot \xi \cdot \sin a5 \cdot L_{ad})^2 + d^2}}{(L_{sa} + L_{ad})}$$

The results for energy resolution and A4 resolution is summarized in the table below. As evident, there is no discernible difference in energy resolution between short, symmetric and long Q-channels. However, the scattering angle resolution varies between 5 and 7.5 % within the short, symmetric and long variants of a single energy. This is not too much, and it becomes even less when is the Q-resolution of the spectrometer as a whole is considered. The incoming

beam divergence of 0.5-1.5 degrees, makes these differences in the few percent range. This effect is not large, as asymmetries in sample mosaicity, variations in mosaicity, etc will smooth over such systematic differences anyway.

	L_{sa} [mm]	L_{ad} [mm]	Vertical coverage [deg.]	ΔA4 [deg]	ΔE_{tube} [μeV]	$\Delta E_{triplet}$ [μeV]
2.7 meV - short	1100	1189	2	0.89228	23	60.3
2.7 meV – symm.	1189	1189	2	0.85889	22.6	60
2.7 meV - long	1276	1189	2	0.82857	22.5	59.7
3.2 meV - short	1238	1314	1.8372	0.81187	30	80
3.2 meV – symm.	1314	1314	1.8372	0.78781	30	80
3.2 meV - long	1388	1314	1.8372	0.7657	30	80
3.8 meV - short	1342	1418	1.6861	0.74399	40	106
3.8 meV – symm.	1418	1418	1.6861	0.72356	39	105
3.8 meV – long	1493	1418	1.6861	0.70446	39	105
4.4 meV - short	1443	1520	1.5669	0.69039	49	131
4.4 meV – symm.	1520	1520	1.5669	0.67269	48	130
4.4 meV – long	1595	1520	1.5669	0.65587	48	130
5.0 meV - short	1544	1622	1.47	0.64672	58	155
5.0 meV – symm.	1622	1622	1.47	0.63098	57	155
5.0 meV – long	1697	1622	1.47	0.61618	57	154

Table 2: Analyser performance, using a sample size of 5 mm

In conclusion, our choice of analyser arrangement and analyser geometry is buildable, shieldable and performs to the high-level requirements of the Bifrost instrument.

8. APPENDIX A – SUMMARY PLOTS

Here follows the summary plots for all planned analysers. The blue dashed line is the simulated optimum. As evident, the analysers are well understood and the calculated optima are in agreement with the simulated ones.

8.1 Summary plots for 2.7 meV

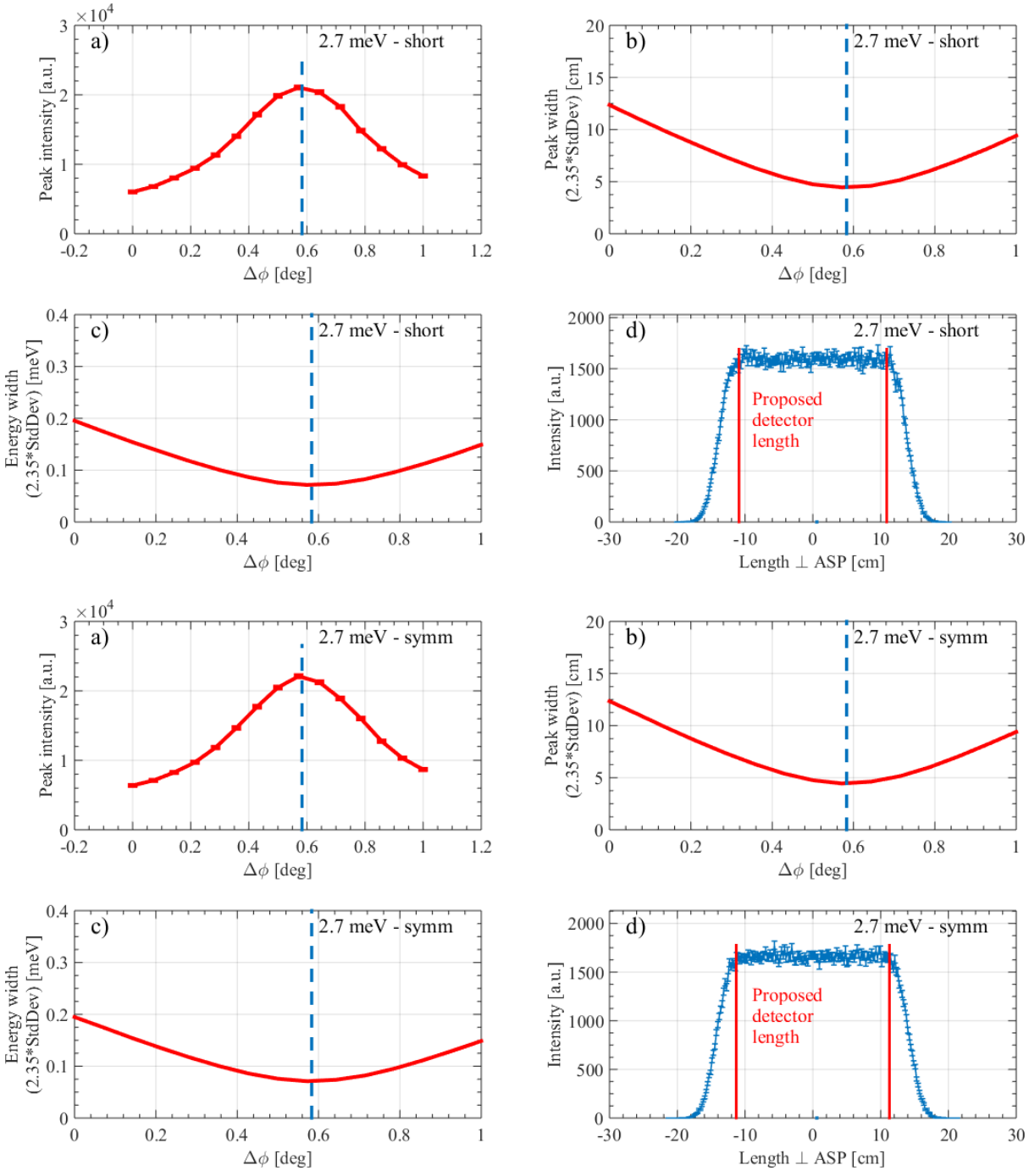

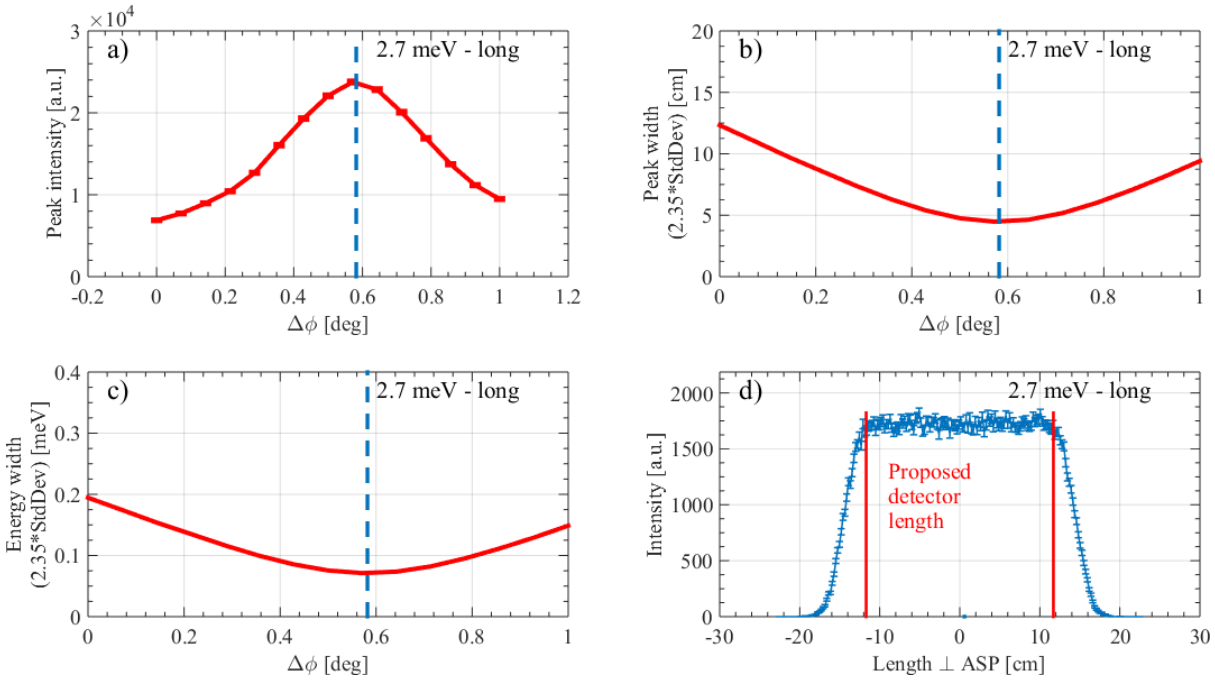

8.2 Summary plots for 3.2 meV

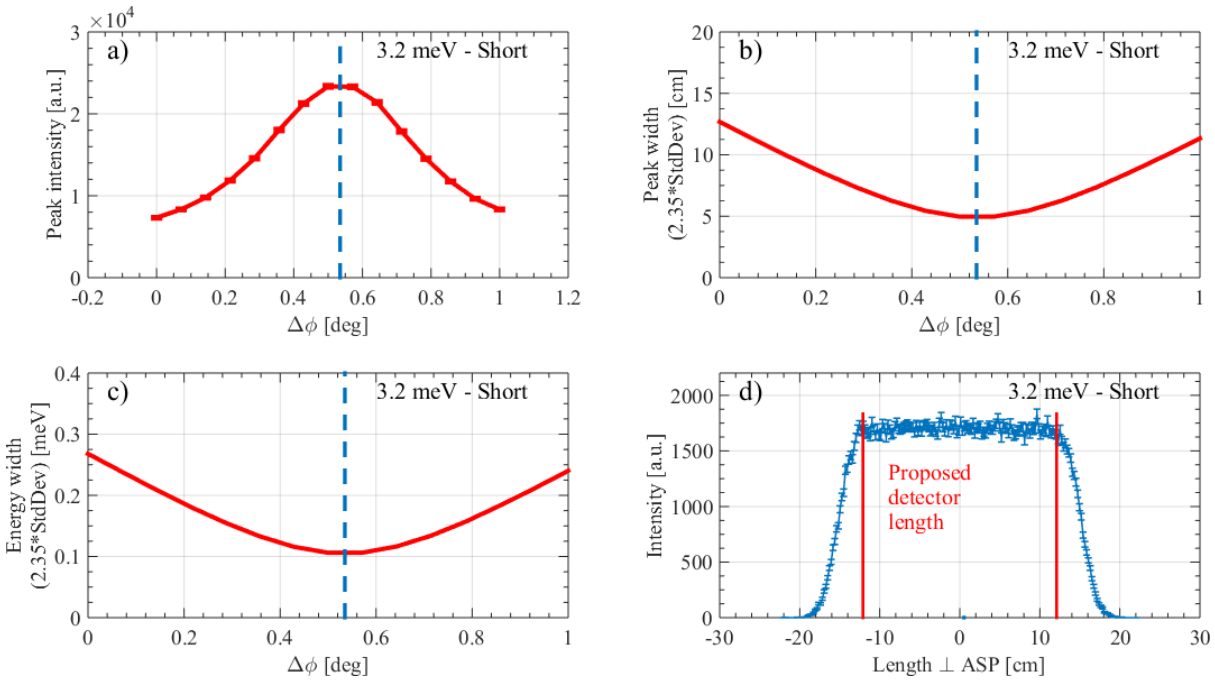

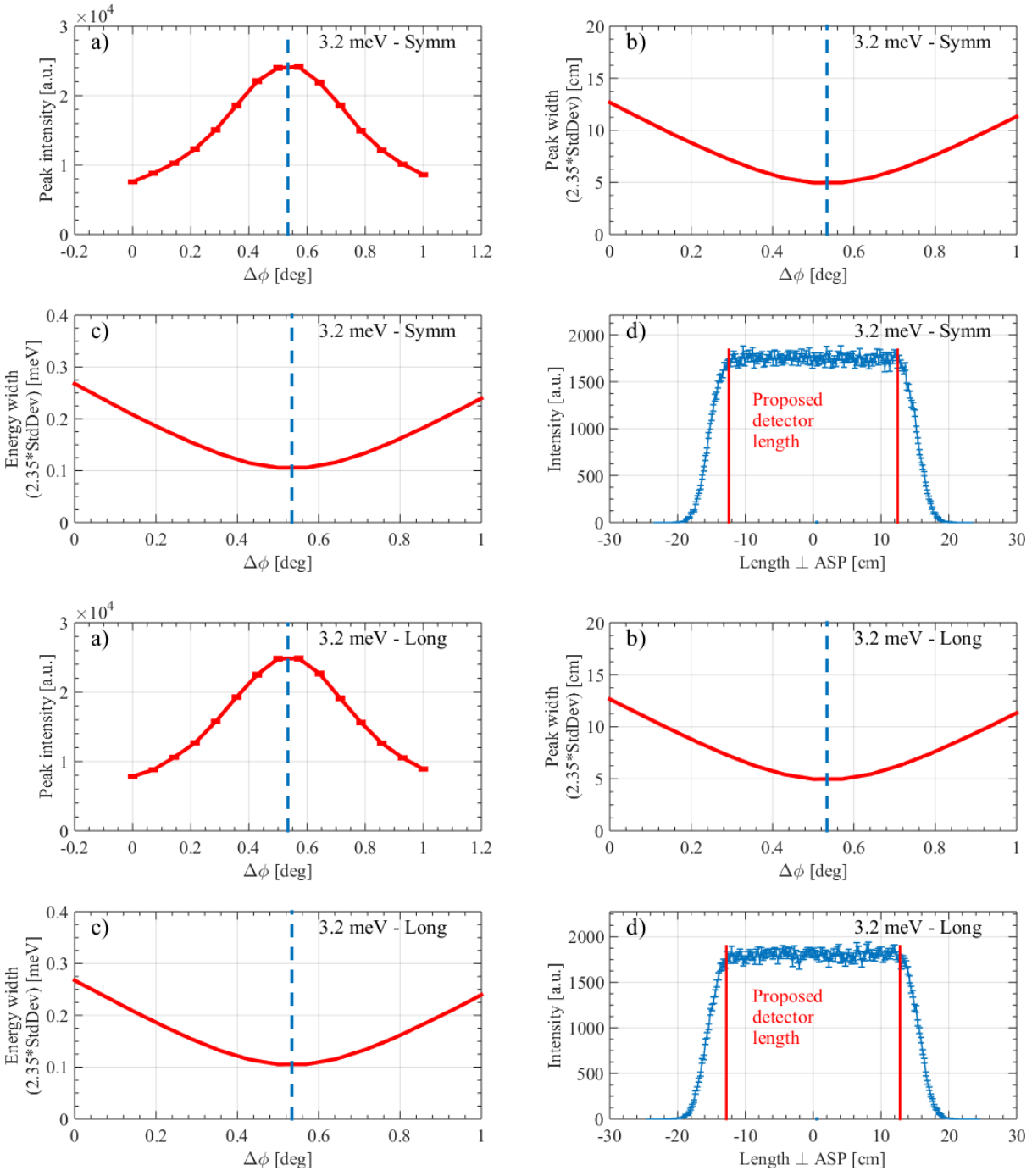
a)
3.2 meV - Symm
Peak intensity [a.u.]
Δφ [deg]
b)
3.2 meV - Symm
Peak width (2.35*StdDev) [cm]
Δφ [deg]
c)
3.2 meV - Symm
Energy width (2.35*StdDev) [meV]
Δφ [deg]
d)
3.2 meV - Symm
Proposed detector length
Intensity [a.u.]
Length ⊥ ASP [cm]
a)
3.2 meV - Long
Peak intensity [a.u.]
Δφ [deg]
b)
3.2 meV - Long
Peak width (2.35*StdDev) [cm]
Δφ [deg]
c)
3.2 meV - Long
Energy width (2.35*StdDev) [meV]
Δφ [deg]
d)
3.2 meV - Long
Proposed detector length
Intensity [a.u.]
Length ⊥ ASP [cm]

8.3 Summary plots for 3.8 meV

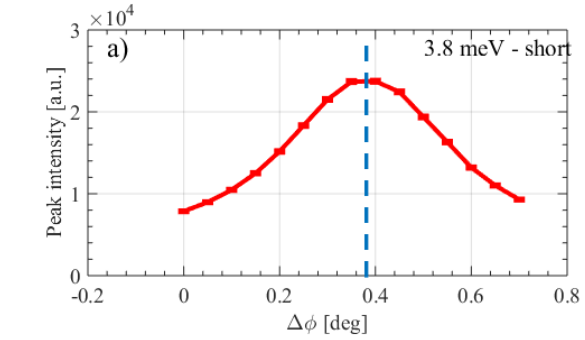

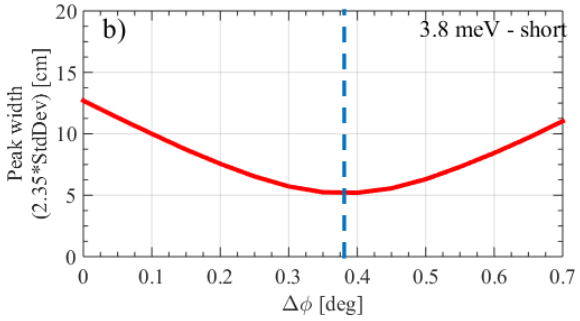

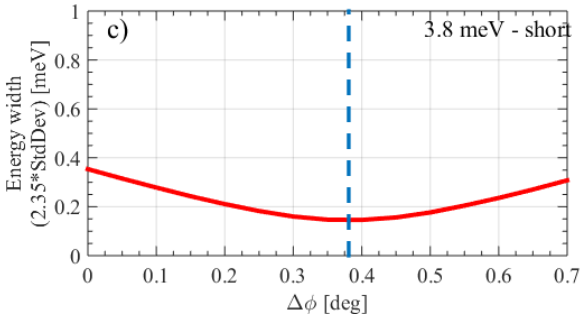

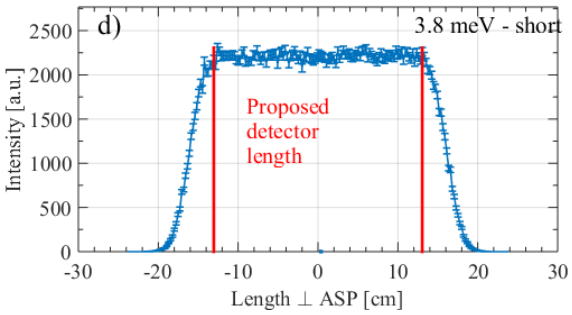

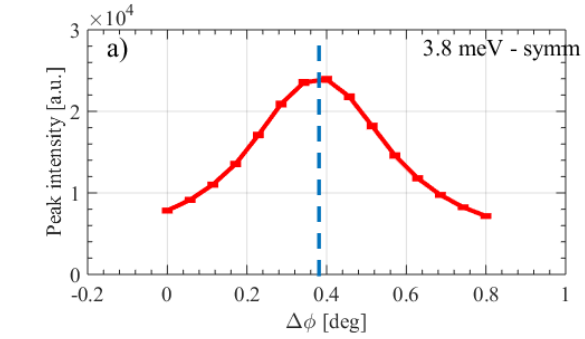

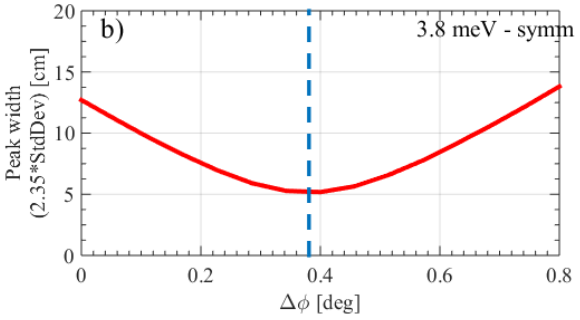

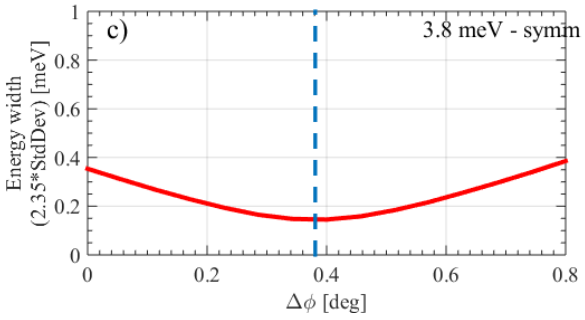

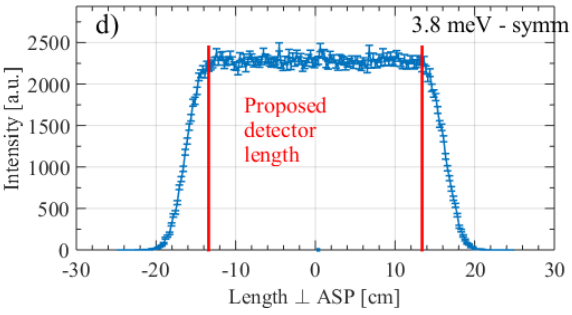

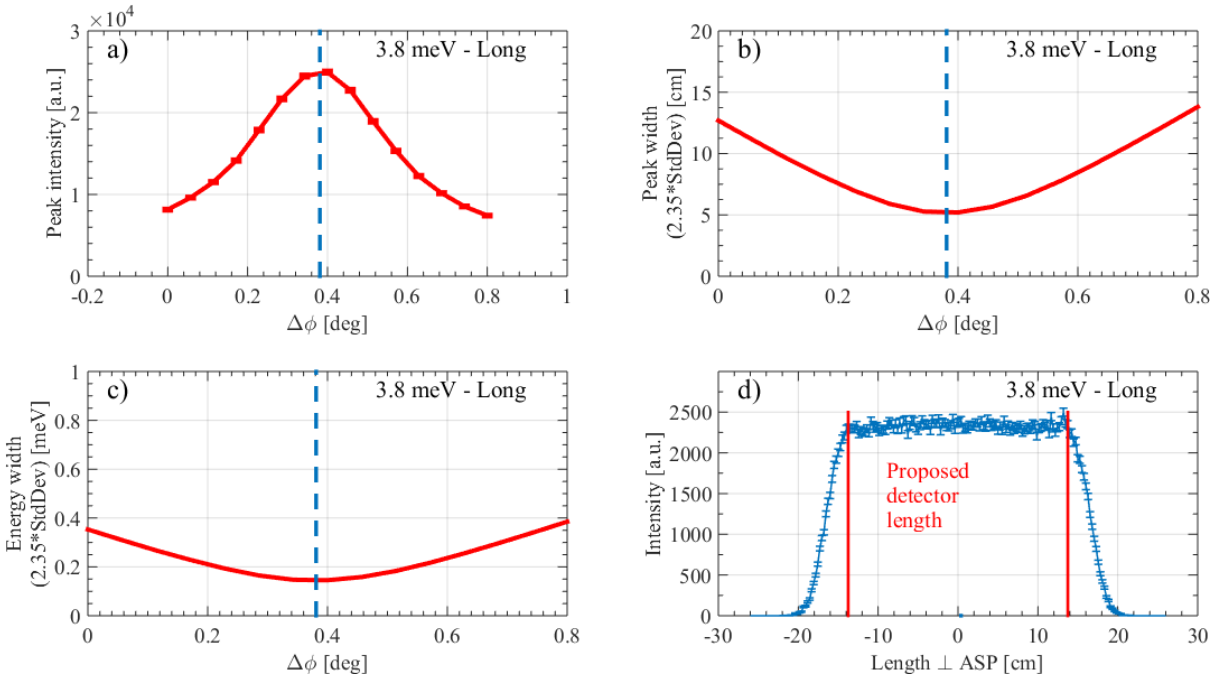

8.4 Summary plots for 4.4 meV

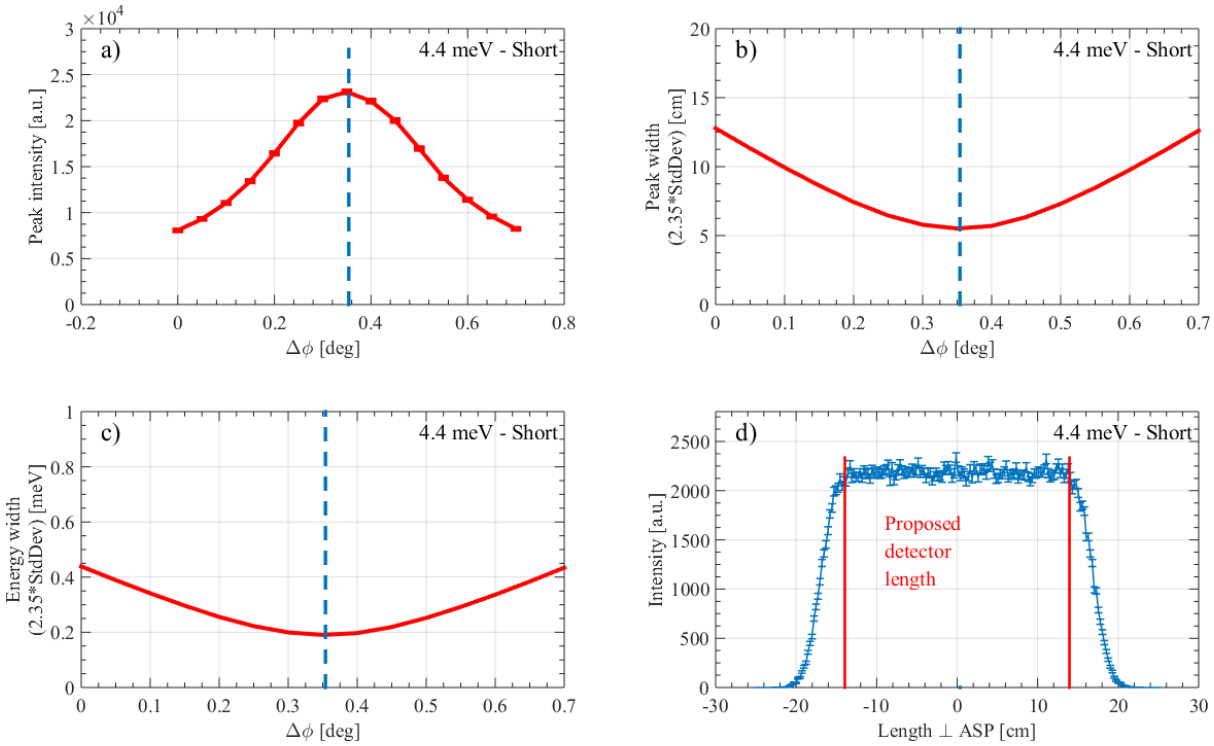

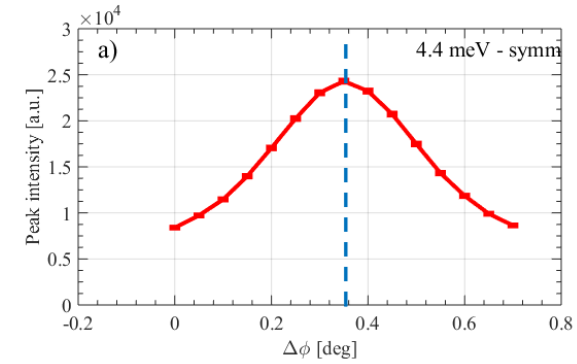
a)
4.4 meV - symm
×10^4
Peak intensity [a.u.]
Δφ [deg]

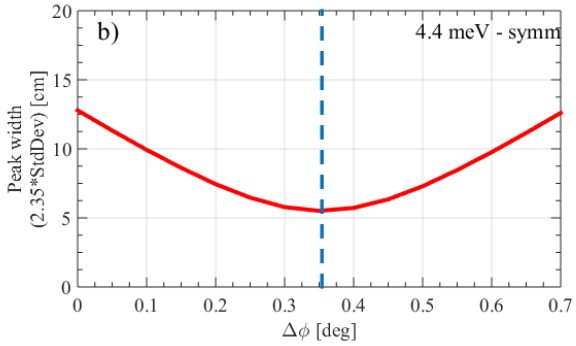
b)
4.4 meV - symm
Peak width (2.35*StdDev) [cm]
Δφ [deg]

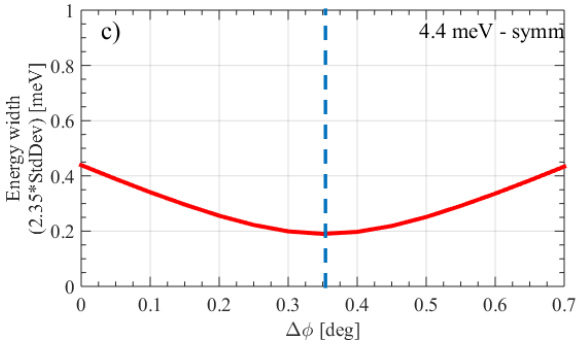
c)
4.4 meV - symm
Energy width (2.35*StdDev) [meV]
Δφ [deg]

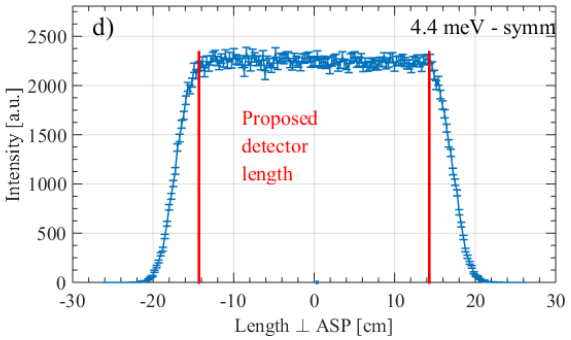
d)
4.4 meV - symm
Proposed detector length
Intensity [a.u.]
Length ⊥ ASP [cm]

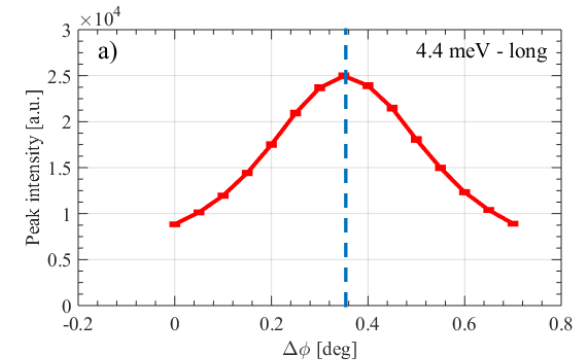
a)
4.4 meV - long
×10^4
Peak intensity [a.u.]
Δφ [deg]

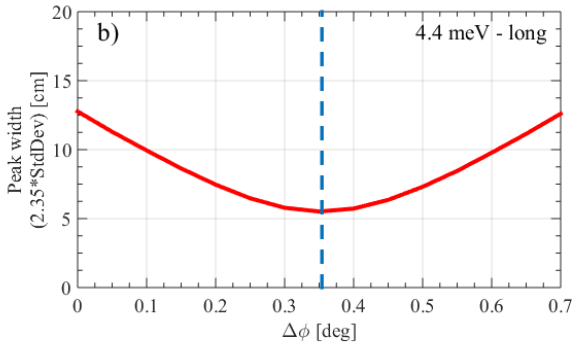
b)
4.4 meV - long
Peak width (2.35*StdDev) [cm]
Δφ [deg]

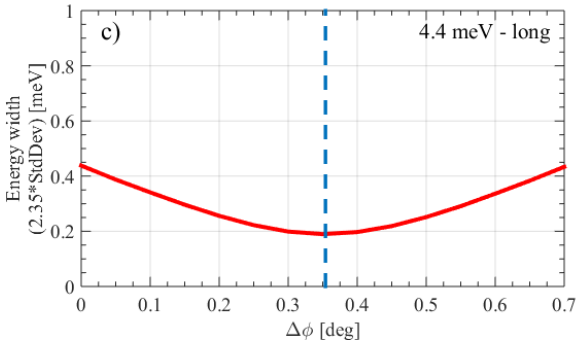
c)
4.4 meV - long
Energy width (2.35*StdDev) [meV]
Δφ [deg]

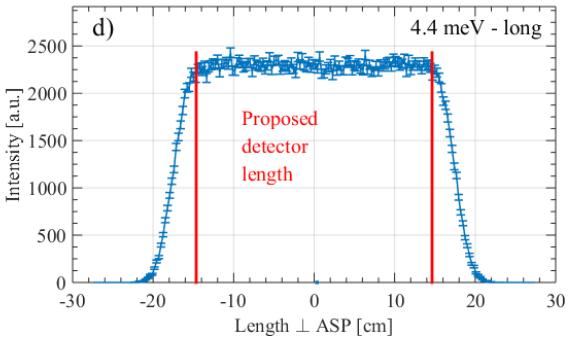
d)
4.4 meV - long
Proposed detector length
Intensity [a.u.]
Length ⊥ ASP [cm]

8.5 Summary plots for 5 meV

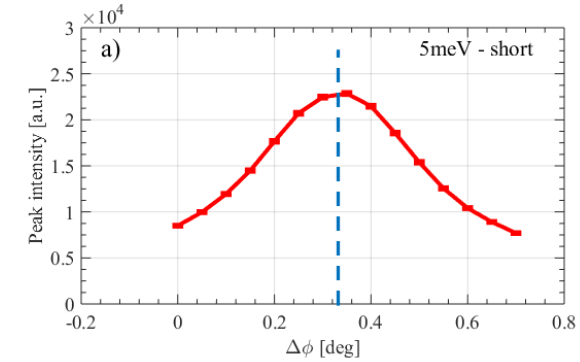

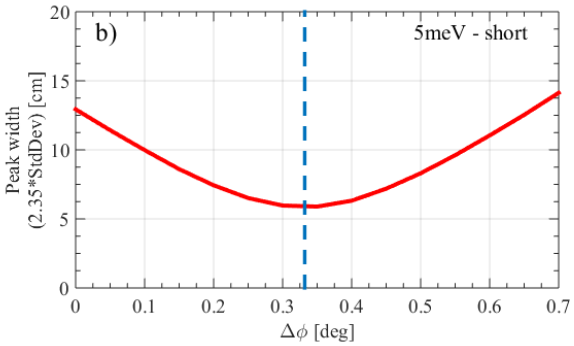

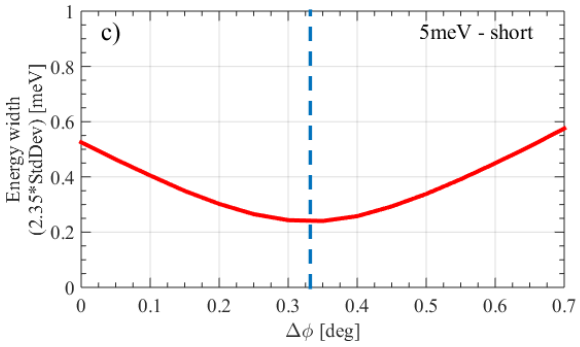

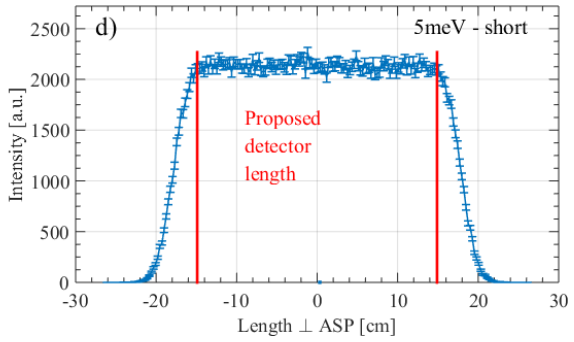

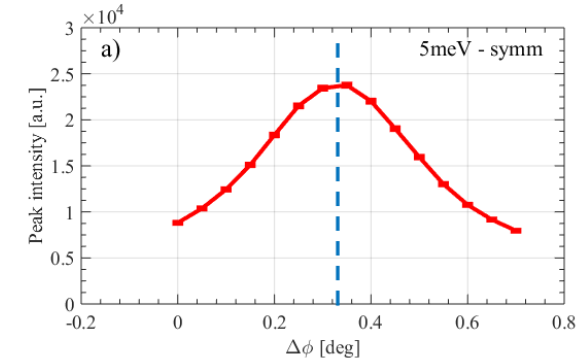

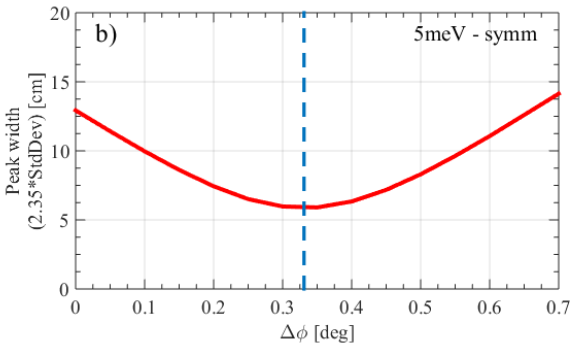

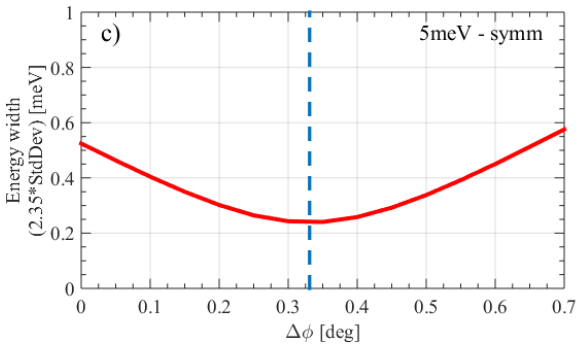

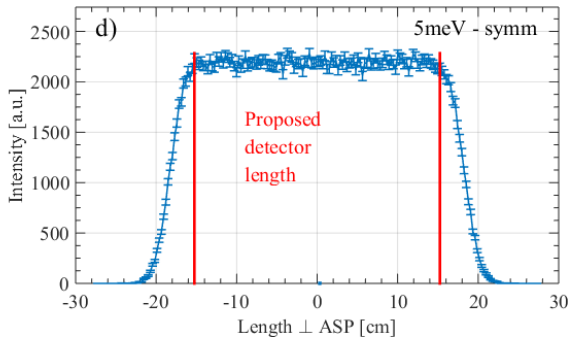

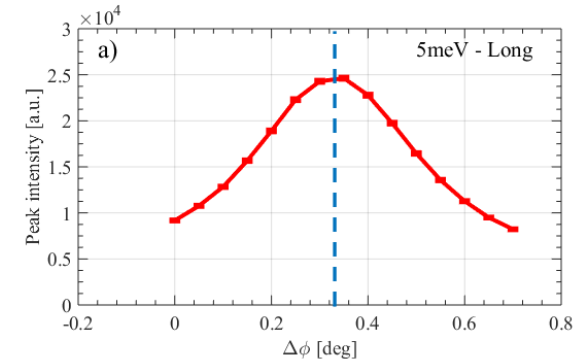
a)
5meV - Long
×10^4
Peak intensity [a.u.]
Δφ [deg]

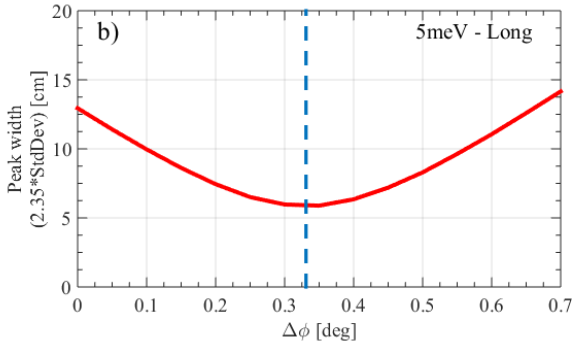
b)
5meV - Long
Peak width
(2.35*StdDev) [cm]
Δφ [deg]

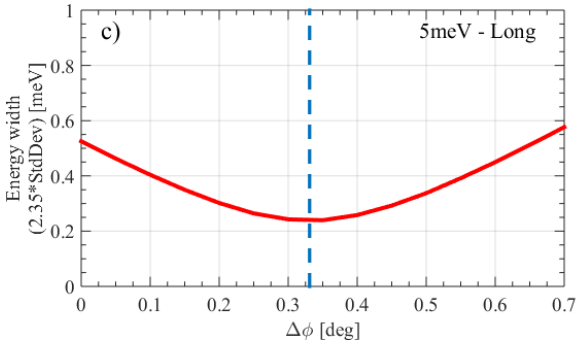
c)
5meV - Long
Energy width
(2.35*StdDev) [meV]
Δφ [deg]

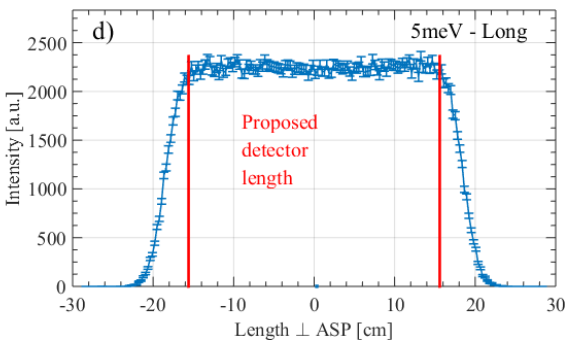
d)
5meV - Long
Proposed
detector
length
Intensity [a.u.]
Length ⊥ ASP [cm]